Report No. 179 / UILU ENG-98-4007

Effects of Rail-End Beveling on Thermite Welding

A Research Report to the Association of American Railroads

by

Jeffrey N. Withee
Frederick V. Lawrence

Department of Civil and Environmental Engineering
University of Illinois at Urbana-Champaign

Urbana, Illinois
May 1998

EFFECTS OF RAIL-END BEVELING ON THERMITE WELDING

Thermite welds were fabricated using standard, squeezed, and vibrated weld methods and evaluated to determine the benefits of rail end beveling. The rail end beveling consisted of trimming back the rail base. The rail trimming was performed so that base metal to base metal contact would occur in the rail head of the squeezed weld. Welding was completed on an I-beam fixture having a hydraulic ram that allowed a squeeze force or vibration to be introduced during weld solidification. Three types of welds (standard, squeezed and vibrated) were created for testing. Standard welding required no ram movement, squeezed welding brought the rail ends together until a set compressive force was achieved, and the vibrated weld involved vibrating the weld metal with the ram until a measurable resistance occurred.

The welds were tested and examined to determine tensile properties, hardness, fatigue life, porosity (using confocal microscopy), and weld microstructure. The squeezed weld with the rail end beveling treatment achieved base metal to base metal contact in the rail head and a smaller overall width of weld metal than the other two weld types. Squeezed and vibrated weld metal exhibited lower porosity than the standard weld metal. The squeezed weld exhibited fatigue performance superior to both the standard and vibrated welds. No notable differences were observed in tensile and hardness measurements made on the three welds. Squeezed welding improved weld properties by expelling thermite metal and reducing the size of the largest pore.

ACKNOWLEDGMENTS

This research project is a continuation of previous work on the improvement of thermite welding of railroad rail. This and previous work on the subject was sponsored by the Association of American Railroads. Orgo-Thermit, Inc. of Lakehurst, NJ donated the welding equipment used in this study.

The authors would like to thank Mr. Jian Sun of the Association of American Railroads for hosting a visit to the Transportation Technology Center in Pueblo, Colorado and Mr. Cameron Lonsdale of Conrail for assisting me with some helpful advice and background literature.

TABLE OF CONTENTS

LIST OF TABLES

LIST OF FIGURES

1.0 INTRODUCTION

1.1 Motivation for Thermite Welding Research

Thermite welds are easily created, but suffer from poor fatigue performance especially under the new heavy axle loads that railroads are employing for reasons of economy. Three major advantages of thermite welds are portability, low equipment cost, and brief rail traffic interruption (Gibert, 1988). A high failure rate is the main weakness of thermite welds (Hauser, 1978). Improvements in thermite weld quality have been made, but there is room for more work to be done (Railway Track & Structures, 1990) and (Kramer, 1996). New thermite welding procedures must not sacrifice the simplicity that makes thermite welding the best choice in certain track welding situations.

1.2 Process Basics and History

Thermite welding has been a proven industrial process since 1898 (Moin, 1988) and was applied to rails as early as 1906 (Gibert, 1988). The thermite reaction is based on the use of aluminum to reduce iron oxide. A common reaction equation is given by Fricke (1984) as :

$$3Fe_3O_4 + 8Al \rightarrow 9Fe + 4Al_2O_3 + \Delta H; \qquad \Delta H = \text{energy released} = 3350 \text{ kJ}$$

Exact reaction equations vary depending on manufacturer (Hauser, 1978). All of the reactions are highly exothermic and the resultant liquid iron can reach temperatures of 2400-2800°C (Gibert, 1988). The by-product of this reaction, aluminum oxide slag (Al_2O_3), is also liquid at these temperatures. Certain alloying elements are included in the thermite charge to yield a filler metal that has the appropriate rail steel chemistry. Specific alloying elements and quantities in each charge vary depending on the manufacturer and type of rail being welded. Using an appropriate reaction crucible and mold, the liquid steel can be poured in between rail ends to form the weld. The slag is lighter than the steel and

therefore will float on top of the molten steel. This separation ideally leaves only steel in the mold to cool and form the rail weld. For a more detailed discussion of the thermite welding process, see Key (1984).

1.3 Previous Research Work

Commercial manufacturers have been working to improve the chemistry of thermite charges to match rail base metal. Post-weld heat treatments have also been developed to yield microstructure improvements over the as cast welds (Railway Track & Structures, 1990) and (Kramer, 1996). An example of this type of process involves setting a mold around the completed weld that prevents the thermite metal from directly contacting the weld, but allows the heat from a small thermite charge to normalize the weld and refine the grain size (Kramer, 1993). Research efforts have also considered the use of filters to reduce the number of alumina inclusions allowed to flow into the rail weld cavity (Schroeder and Poirier, 1985).

Another successful path that has been followed in the effort to improve the properties of thermite rail welds includes methods of physical agitation of the weld metal during solidification. Applying a force to squeeze the rails together is one method that has been tested at the University of Illinois and the Association of American Railroads. Vibration of the rails during weld solidification has been studied as well.

Several researchers have demonstrated that squeeze welding can improve a number of weld properties. At the University of Illinois at Urbana-Champaign, Fry (1992) reported that tensile strength and elongation were greater for a squeezed weld than for a standard thermite weld. In addition, Fry found that weld metal grain size was reduced by the squeezing process. Sun and co-workers (1994) from the Association of American Railroads (AAR) also reported squeezed weld improvements to mechanical properties, including fatigue performance. Metallurgical benefits of fewer inclusions were reported by researchers from AAR. Liu (1994) from the University of Illinois performed additional

experiments that support the AAR results that squeezing benefits mechanical and metallurgical properties. Squeezing was accomplished using a hydraulic ram on an I-beam fixture at the University of Illinois and rail pullers in the work done by AAR. The use of a hydraulic ram allowed Liu to superimpose a vibrational motion on the squeezing action during weld solidification. Liu (1994) found this squeezed and vibrated weld to yield the best fatigue performance.

Three different researchers have recently studied the effect of vibration alone on thermite welds. Siska (1980) found that sonic vibration caused grain refinement and an equiaxed microstructure. These microstructure benefits were usually only realized on the side of the weld being vibrated. Strength and ductility gains were seen by Lonsdale (1992) after vibrating a full thermite rail weld for one and a half minutes four minutes after pour completion. Lonsdale did not observe any change in grain size due to the applied vibration. Liu (1994) studied pure vibration and found that fatigue performance improved over standard thermite welds, but did not equal or exceed squeezed or squeezed-vibrated weld data.

1.4 Project Scope

The goal of this research was to develop procedures that improve the mechanical performance of thermite welds. To achieve this goal, three welding methods (standard, squeezed, and vibrated) were used to join rails whose ends had been beveled. The completed welds were evaluated mechanically and metallographically to determine the effectiveness of rail end beveling.

2.0 PROCEDURES

2.1 Experimental Setup

All welds in this study were made using 136RE standard rails. Each weld joined two segments of rail, each approximately 1 m in length. The thermite welds were made with Standard SKV-F Thermit® Welding Kits from Orgo-Thermit, Inc. Unless otherwise noted, the manufacturer's recommended procedures were followed.

The rails to be welded were placed on a steel I-beam with guides to ensure alignment in the horizontal and vertical planes. One rail was kept stationary and the other was attached to a hydraulic ram that generated the force or vibration on the weld metal during solidification. Figure 1 is a schematic representation of the I-beam fixture. In this study, the ram was controlled by a newly developed Labview computer program capable of force and displacement control modes. For squeezed welding, a set force can be applied, a set displacement can be imposed, or a displacement rate can be followed up to a displacement limit or a maximum force. Sine or haversine wave functions can be applied with user-defined amplitudes and frequencies to vibrate the weld. A combined squeezed and vibrated weld is possible by superposing a wave function on a constant rate of displacement.

2.2 Modified Procedures

The set of experimental welds differed from the standard thermite welding procedures in two respects: all rail-ends were beveled and some welds were squeezed or vibrated during weld metal solidification. Previous experiments with squeezed welding demonstrated that faster solidification in the rail base caused the first contact to occur in the rail base. The rail ends for this series of tests were beveled to force first contact in the rail head. The ends of both rails were beveled at the base as shown in Figure 2. The initial gap between the rail heads was reduced to 19 mm from the standard 25 mm to allow the

standard ceramic molds to completely enclose the rail gap. Even with the reduced initial gap at the rail head the gap at the bottom of the rail base was 51 mm. This rail gap and the rail end beveling required the thermite charge to fill a volume larger than the volume for which it was designed.

The hydraulic ram on the I-beam welding fixture permitted the squeezing of the rail ends together or vibration of one rail during weld solidification. Two welds with no ram activity (standard), one squeezed weld, and one vibrated weld were fabricated.[1] Special, but effective, precautions developed in a previous study (Fry, 1992) prevented the crumbling of luting sand and consequent leaking of liquid thermite metal when the rails were translated during squeezing. A pair of concrete blocks that conform to the rail were clamped between the mold and the universal clamp to help the mold resist motion (translation and rotation) during rail movement and to contain the luting sand. An aluminum plate was attached to the mold shoes to contain the luting sand on the other side of the mold. Figure 3 shows this area of the test setup immediately after welding. Squeezing and vibration sequences were started immediately upon completion of the liquid thermite pour. The squeezing ram program used displacement control to bring the rails together until a force limit triggered a switch to load control. The squeezing force was held for two minutes after the maximum force limit was achieved. The maximum applied force was low (29 kN) when compared with previous squeezed welds of 182 kN (Fry, 1992) and 356-534 kN (Sun et al., 1994). The low force allowed the use of a smaller, less expensive apparatus and helped reduce the potential for rail misalignment that has been a concern of others (Sun et al., 1994). The vibration sequence used a haversine wave in displacement control and was stopped when the measured force approached 0.9 kN to avoid damaging the weld through introduction of hot tears (Siska, 1980). Table 1 contains all pertinent information about compressive force used, duration of ram activity, and

[1] One of the standard welds contained an unacceptable level of porosity and therefore was not included in the analysis. The reason for the unacceptable, gross amount of porosity was unclear because all proper welding procedures were followed during weld fabrication.

frequency of vibration, where appropriate. A graph of compressive force and ram position for the squeezed weld is given in Figure 4.

2.3 Chemical Analysis

Samples of rail base metal and metal from the three completed welds were sent to Chicago Spectro Service Laboratory, Inc. for chemical analysis. The weld samples were all taken from the rail head across the weld centerline. The chemical compositions are listed in Table 2. Of principal interest is the aluminum content which is a result of the alumina inclusions that contaminate the weld as a by-product of the thermite reaction. The lowest values were present in the base metal and squeezed weld with the vibrated and standard welds following in order of increasing aluminum content. The squeezed weld metal chemistry closely followed the base metal chemistry because the squeezing procedure expelled most weld metal from the rail head, and therefore, the sample analyzed contained both weld metal and base metal.

2.4 Porosity Counting with Confocal Microscopy

Two samples for quantitative metallography measurements were cut from each weld. The two samples permitted porosity counting on the transverse and longitudinal faces of the cast weld metal. These samples were from Position 9 shown in Figure 5. The orientation of the transverse (W) and longitudinal (L) faces with respect to the rail weld are shown in Figure 6 where T is the top of the rail. Two specimens of this type were obtained from each weld, one on either side of the transverse weld centerline. These specimens were then polished using standard metallographic procedures. One specimen was polished on the W face, and the other specimen was polished on the L face.

Porosity was measured on the polished and unetched samples using a Zeiss Laser-Scanning Confocal Microscope. Confocal microscopy is capable of sharper images and greater depth resolution than standard optical microscopy. An external argon laser with a

488 nm wavelength was used as the light source. Four different sites of each sample were scanned for porosity using the confocal microscope for a total area assayed of 3.53 mm^2 per specimen face. The data from the confocal microscope consisted of eight digital images (four transverse and four longitudinal) for each weld. The digital images contained surface height information in the form of intensity values such that darker portions of the image (lower intensity) corresponded to lower areas on the surface. The image was stored as a 512 x 512 grid of points or pixels each with a known intensity. Additional discussion on the use of confocal microscopy to measure surface features is given in Lange, Jennings, and Shah (1993).

The confocal images were then analyzed using a public domain software package developed at the National Institutes of Health entitled NIH Image. After importing the confocal image, a threshold value of the pixel intensity was determined. The software false-colored regions that fell below the threshold so that one could see which areas of the image would be counted as porosity for the threshold level chosen. The appropriate threshold was determined by choosing the highest value that did not result in flat areas of the specimen surface being counted as porosity. Using software subroutines, all pixels darker than the threshold value (pixels representing porosity) were counted. The percent porosity was simply the number of porosity pixels divided by the total number of pixels in the image. The four measurements from each specimen were averaged to achieve a transverse and longitudinal porosity measurement for each weld.

2.5 Tensile Tests

Tensile tests were performed using a servo-hydraulic loading frame. The testing was completed in strain-control mode with the ram program and data acquisition run through a computer control program developed in Labview. Elongation was measured over a 25.4 mm gage length. Two tensile specimens were machined from the head of the rail as shown in Figure 5 which details the location of all specimens. The lengths were cut

such that weld metal was within the reduced section of the specimen. The specimen dimensions for tensile testing are shown in Figure 7.

2.6 Hardness Tests

Vickers Micro-Hardness tests were performed on the base metal, weld metal, and heat affected zone of each weld. Four determinations of hardness were made in each of the three locations using a Leitz-Wetzlar Miniload Hardness Tester.

2.7 Rotating Bending Fatigue Tests and Fracture Evaluations

Fatigue specimens from the rail welds were tested in an R.R. Moore type rotating bending fatigue machine. The rotation speed averaged 2,500 rpm. Cycles were reported in increments of 1,000. The number of cycles to failure and the maximum stress in the outer fiber of the specimen were recorded for each test. A runout was declared when the cycle counter reached or exceeded $3x10^7$ cycles.

Figure 8 shows the dimensions for the cylindrical specimens used in the fatigue testing. Fatigue specimens labeled 1-6 in Figure 5 were tested for each weld. A second set of six fatigue specimens was machined from the squeezed weld because the first set contained HAZ in the specimen gage section, not weld metal. A mechanical displacement of the weld zone caused by the squeeze welding (see Section 3.1) was the cause of the misalignment. The second set of squeezed specimens was more carefully machined so that the center of the fatigue specimen contained weld metal. Unfortunately, the second set of squeezed specimens had to be cut from the upper web area around and including specimen Number 10 in Figure 5 rather than from the rail head. However, all specimens were taken from the non-beveled region of the rail (top 96 mm of the rail as shown in Figure 2.) After failure, representatives of the second set of fatigue specimens were mounted, polished, and etched to verify that failure occurred in the weld metal.

A number of fatigue specimen fracture surfaces were investigated with a Hitachi

S-570 Scanning Electron Microscope to locate and evaluate the pores initiating failure. Optical micrographs were also taken of representative fracture surfaces.

3.0 RESULTS

3.1 Metallographic Observations

Metallographic cross-sections that include the weld (base metal to base metal) from Position 10 in Figure 5 were photographed. Tracings of the micrographs are shown in Figure 9. The extent of weld metal (WM), the heat affected zone (HAZ), and the centerline of the mold during welding are indicated below each tracing. The standard weld (Figure 9a) had the typical width of weld metal, and its HAZ centered about the mold cavity. Comparing Figure 9a and Figure 9c shows that the vibrated weld had the same HAZ and weld metal pattern as the standard weld.

The squeezed weld had a reduced volume of weld metal, an asymmetric HAZ, and a shift in the weld metal centerline. The volume of the squeezed weld metal was smaller than the standard and vibrated welds because of the squeezing during solidification. The weld metal was shifted to the left so it was no longer in the center of the mold cavity. The moving rail (on rollers in Figure 1) was on the right, and displacement was applied from right to left in Figure 9b.

Figure 10 shows an estimated squeezed weld profile based on the measurement of the weld metal width on the first set of fatigue specimens and the metallographic sample (Positions 2, 3, 6 and 10 in Figure 5.) Base metal (BM) to base metal contact is evident in the rail head. This BM to BM contact was observed in fatigue specimen Number 6.

Figures 11-13 are micrographs of weld metal for the standard, squeezed, and vibrated welds, respectively. Each figure contains a micrograph of the line of fusion and another micrograph of weld metal. In each figure, the dendritic structure of the weld metal is clearly seen in comparison to the base metal heat affected zone. Comparison of Figures 11b, 12b, and 13b reveals a refined grain size in the squeezed weld metal. Using a circular intercept counting procedure to quantify average grain diameter indicated that the grains in the standard and vibrated welds were 2-3 times larger than the grains in the squeezed weld.

3.2 Porosity Measurements

A representative confocal image of the standard weld is shown in Figure 14. The image shows lower surface areas as darker regions. The weld pores appear as surface pits and are therefore the darkest areas on the image. Figures 15 and 16 are confocal images of the squeezed and vibrated welds respectively. The four confocal microscopy measurements taken on each specimen are averaged and reported in Table 3. The data for the transverse face of the squeezed weld was unavailable due to the problems with the displacement of the weld zone.

Measurement of the three welds demonstrated that the standard weld had the highest porosity with a value of 0.41%. The squeezed weld (0.23%) and vibrated weld (0.16%) had lower porosity than the standard weld. Values were consistent between the transverse and longitudinal faces. An average of 1,000 pores from each weld were counted to determine the pore size distributions. Figure 17 shows that all three welds had similar pore-size distributions. It is important to note that Figure 17 gives no information on total amounts of porosity (see Table 3) as the vertical axis is the probability of finding a certain size pore.

As seen in Figure 17, the actual observed pores causing fatigue failure were much larger than the largest pore observed in the porosity distributions. This result is reasonable because the largest pore present will initiate failure. These large-failure causing pores are so few in number that virtually the entire specimen surface would have to be examined to find them. It is possible that the size distributions in Figure 17 may be skewed toward smaller pores due to the automated pore counting software's inability to determine that a pore cluster is in fact a single, large pore complex. The program may count adjacent areas of porosity as multiple small pores when they are in fact one, large pore.

3.3 Tensile Tests

Two tensile specimens were tested from each of the standard, squeezed, and

vibrated welds. The weld metal of the squeezed weld was not in the clip gage length due to the displacement of the weld zone discussed in Section 3.1. However, the squeezed weld metal was contained in the reduced section of the tensile specimen, and failure did occur in the weld metal. Therefore, modulus and yield data presented for the squeezed weld are from the HAZ, but the ultimate tensile strength is representative of the weld metal. All data from the standard and vibrated welds are representative of weld metal.

Table 4 lists the modulus of elasticity, yield stress, ultimate stress, and maximum elongation for the six specimens. All three welds, standard, squeezed, and vibrated, showed very similar average tensile properties. The average elongations were virtually identical; however, the two test values from the squeezed weld were determined by fractures outside of the gage length. Stress-strain plots obtained during the tensile tests are shown in Figure 18. The two specimens from the standard weld exhibited virtually identical stress-strain characteristics. The data reveal that there was no appreciable difference in tensile properties of the three welds.

3.4 Hardness Tests

The standard, squeezed, and vibrated welds were tested for Vickers Micro-Hardness. The results in Table 5 show the values for base metal, weld metal and heat affected zone (HAZ). The average base metal hardness of 346 HV was the same for each weld type. In all three cases, the HAZ was the hardest material followed by the weld metal. The standard, squeezed, and vibrated welds exhibited similar weld metal and HAZ hardnesses.

3.5 Fatigue Tests

The fatigue data are listed in Table 6 and are plotted in Figure 19.[2] The open

[2] Fatigue specimens from the fabricated welds were tested in rotating bending. The results referred to as "squeezed weld" in this section are from tests of the second set of specimens as discussed in Section 2.7 and shown in Figure 10.

symbols are specimen failures and the shaded symbols are discontinued tests or "runouts." The squeezed weld data exceeded that of the other weld types. A runout was obtained at a maximum stress of 413 MPa. There was also a failure at 441 MPa of 2.33×10^5 cycles. The other weld types experienced failures for similar cycle counts (3×10^5-5×10^5) in the 330-345 MPa range. Runouts from the standard weld and vibrated weld were obtained at stresses of 290 MPa and 276 MPa respectively.

Figure 20 compares the fatigue data from this test series with previous work by Liu (1994) who performed similar modified welding procedures. The current squeezed weld data agrees with Liu's. The standard and vibrated weld data show the same fatigue life trends of Liu's data.

3.6 Fractography

Optical fracture surface images for the three weld types are shown in Figure 21. A single fatigue failure initiation site is apparent in each of the three images in Figure 21. The sizes of pores initiating failure were quantified on seven fracture surfaces. A scanning electron microscope (SEM) was used to identify pores on two standard weld specimens, four squeezed weld specimens, and one vibrated weld specimen. Figures 22 through 28 are the SEM micrographs of the pores initiating fatigue failure. Pores were categorized as spherical pores or shrinkage pores. Spherical pores had an elliptical or circular shape, while shrinkage pores exhibited an irregular outline. Shrinkage pores were more common with specimens B1 and B4 (Figures 24 and 27) being the only spherical pores. An effective radius for each pore was measured depending on the pore type. The radii of spherical pores were defined as the radius of the circular area or the average radius of the elliptical area of the pore. The radii of shrinkage pores were defined as the radius of the smallest semi-circular area extending in from the specimen surface and containing the entire pore (Siljander and Lawrence, 1988). Measured pore radii, calculated equivalent areas, and pore types are reported in Table 7.

4.0 DISCUSSION

4.1 Confocal Microscopy

Measuring porosity by confocal microscopy has numerous advantages over traditional manual point counting techniques. The confocal microscope produces a digital image which simplifies storage, reproduction, and re-evaluation. Computer analysis of the image is faster and more reliable than a person employing point counting techniques. Currently available software allows the user to specify a wide variety of options for the thresholding operation. When used properly, confocal microscopy and electronic image analysis provide a more efficient and reliable porosity counting method than traditional manual counting techniques.

Obtaining a perfectly flat surface is the most important issue in assuring accuracy in counting porosity on a polished section. Achieving this flat surface depends upon: polishing procedures, mounting of the specimen on the stage, and choice of scan area. The area scanned per image must be balanced between the competing factors of maximizing surface flatness over the scanned area (smaller scan area) and measuring a representative area of the specimen surface (larger scan area). Surface flatness and specimen orientation are important because if any part of the mean specimen surface (surface not a porosity pit) is at the same level as a pit from a higher area of the surface the thresholding in NIH Image will not be able to distinguish between the surface from low areas and the pores located in higher areas.

4.2 Observed Fatigue Behavior

The squeezed weld performed better than either the standard or the vibrated weld. There was no difference between standard and vibrated weld fatigue data plotted in Figure 19. The fatigue improvement in squeezed welds and lack of improvement in vibrated welds will be discussed below.

A first step in determining the cause of the differing fatigue behaviors is to review the metallographic observations of weld cross-sections. As seen in the cross-sections of Figure 9, the volume of weld metal varied between the standard, squeezed, and vibrated welds. The standard and vibrated welds exhibited similar weld volumes. The volume of squeezed weld metal was smaller than that of the standard or vibrated welds. Taking the current standard weld volume as 1.0, the vibrated weld volume was 1.0, and the squeezed weld volume (taking an average width) was 0.2. Previous work by Fry (1992) resulted in a standard weld volume of 0.8 and a squeezed weld volume of 0.2. These results suggest total volume of weld metal under test as a possible factor influencing the fatigue performance of the welds.

Tensile tests, hardness tests, and microstructure investigations were performed to determine any effect that material properties might have had on fatigue performance. The tensile properties and hardness values were essentially identical for all three welds, although a smaller grain size was observed in the squeezed weld. The similarity between welds in tensile and hardness results supports the argument that there was no appreciable difference in material properties. From this evidence, it can be concluded that material properties were not responsible for the different fatigue performance of the welds.

Porosity measurements are another set of experiments that might shed light on the fatigue performance of the welds. Significant differences in total amount of porosity were observed for the three thermite welds fabricated. The procedures used to create the squeezed weld and the vibrated weld proved effective in reducing the porosity of the weld metal. The porosity reductions are quantified in Table 3. While the total amount of porosity varied, there was virtually no difference in the pore size distributions seen in Figure 17. The relevance of total amount of porosity is unclear because both squeezed and vibrated welds had low porosity, but only the squeezed weld exhibited improved fatigue performance.

Fracture surface measurements of pore sizes and calculations of initial stress intensity factors reveal additional information regarding fatigue lives. The values reported in Table 7 and plotted in Figure 29 clearly show a correlation between initial stress intensity factor and fatigue life. When combined with previous analyses, these results demonstrate that the fatigue life was controlled by the maximum pore size and not material properties.

Size effects and porosity reduction are two possible causes of the smaller maximum pore sizes leading to an improved fatigue performance in squeezed welds. Porosity reduction from the squeezing process has been demonstrated in the aforementioned porosity measurements. A reduction in porosity decreases the chance of a large pore being included in a given volume of weld metal. The reduced volume of weld metal in the squeezed weld specimen also lowered the probability of a large pore being present in the material under test. The potential importance of size effects raises the question whether the fatigue improvements observed here in small laboratory specimens would be observed in full size welds.

4.3 Opportunities for Future Improvements

Use of larger thermite charges would ensure a better comparison between standard, squeezed, and vibrated welds with beveled rail ends. The beveled rail end treatment so increased the volume of the cavity that the thermite weld metal required to fill the mold was increased by approximately 15%. The increased weld cavity volume was not a concern in the squeezed weld situation, but may have affected weld quality in both the standard weld and vibrated weld experiments.

Different sizes and shapes of rail end beveling may be used to decrease the volume of weld metal required for the squeezed weld. The size and angle of the rail end bevel used in this study were based on general observations from previous work (Fry 1992). Work on melting and solidification in thermite welds (see Jha, 1989) would be helpful in determining optimal rail end profiles.

Since the highest stresses in a rail are encountered in the head, most efforts have been focused on improving rail head properties. Failures can still initiate in the rail base where there has been less defect detection and improvement effort. The effect of the rail beveling treatment on mechanical and metallurgical properties in the rail base warrants further investigation.

Full scale fatigue tests of squeezed welds should be completed to investigate the role of size effects. The increased volume of weld metal under test in a full rail weld may include larger pores and thus yield no fatigue improvement in squeezed welds.

5.0 CONCLUSIONS

1. Squeezed welds with a rail end beveling treatment achieve base metal to base metal contact in the rail head and a smaller volume of weld metal than standard or vibrated welds. These improvements can be achieved using much lower forces than those previously employed.

2. Confocal microscopy and computer image analysis are reliable and efficient methods for counting porosity when appropriate surface flatness is maintained.

3. Porosity measurements with confocal microscopy demonstrate that squeezed and vibrated welds contain lower weld metal porosity than standard welds.

4. The fatigue properties of thermite rail welds are improved by squeezing the weld during weld solidification. This improvement results from a reduction in the size of the failure initiating (largest) pore.

5. The size of the largest pore or the probability of a certain size pore being incorporated in a test piece is reduced by lowering the general level of porosity and/or by reducing the volume of weld metal under test.

TABLES

Table 1

Experimental Welds and Treatment Parameters

	Standard Weld	Squeezed Weld	Vibrated Weld
Duration of Action (sec.)	-	124	110
Net Rail Displacement (mm)	-	43.7	0
Maximum Compressive Force (kN)	-	28.75	0.89
Vibration Frequency (Hz)	-	-	20
Vibration Amplitude (mm)	-	-	1.27

Table 2

Chemical Compositions

Element	Base Metal	Standard Weld	Squeezed Weld	Vibrated Weld
Carbon (wt. %)	0.77	0.73	0.76	0.73
Manganese (wt. %)	0.80	0.96	0.86	0.96
Phosphorous (wt. %)	0.005	0.023	0.009	0.022
Sulfur (wt. %)	0.013	0.008	0.016	0.013
Silicon (wt. %)	0.24	0.37	0.26	0.41
Nickel (wt. %)	0.09	0.03	0.09	0.02
Chromium (wt. %)	0.21	0.06	0.24	0.07
Molybdenum (wt. %)	< 0.01	< 0.01	< 0.01	< 0.01
Copper (wt. %)	0.25	0.05	0.26	0.06
Aluminum (wt. %)	0.024	0.34	0.025	0.17
Vanadium (wt. %)	< 0.005	0.005	< 0.005	0.005

Table 3

Measured Porosity in Weld Metal

Weld	Transverse Weld Face (W)	Longitudinal Weld Face (L)	Overall Average
Standard			
Porosity (%)	0.37	0.45	0.41
Standard Deviation (%)	0.04	0.05	0.06
Squeezed			
Porosity (%)	-	0.23	0.23
Standard Deviation (%)	-	0.11	0.11
Vibrated			
Porosity (%)	0.14	0.18	0.16
Standard Deviation (%)	0.05	0.07	0.06

Table 4

Tensile Test Results

Weld	Modulus of Elasticity (GPa)	Yield Stress 0.2% offset (MPa)	Ultimate Stress (MPa)	Elongation 25.4 mm gage (%)
Standard (1)	205	605	860	2.6
Standard (2)	208	600	860	2.6
Average	207	603	860	2.6
Squeezed (1)	208	555	905	3.3*
Squeezed (2)	211	555	830	2.3*
Average	210	555	868	2.8
Vibrated (1)	208	595	885	2.9
Vibrated (2)	206	600	845	2.5
Average	207	598	865	2.7

* Fractured outside gage length

Table 5

Vickers Micro-Hardness Test Results

Weld	Base Metal	Weld Metal	Heat Affected Zone
Standard	346	361	390
Squeezed	346	371	380
Vibrated	346	376	383

Table 6

Rotating Bending Fatigue Test Results

Maximum Stress (MPa)	Cycles to Failure
Standard Weld	
345	778,000
331	526,000
331	708,000
317	9,415,000
290	30,064,000+
276	46,020,000+
Squeezed Weld	
469	75,000
441	233,000
428	269,000
427	157,000
413	30,407,000+
400	387,000
Vibrated Weld	
344	348,000
317	554,000
297	2,098,000
276	31,278,000+

+ indicates specimen did not fail

Table 7

Pores Initiating Failure

Specimen†	Pore Radius, r (mm)	Area* (μm^2)	Stress Intensity Factor, K_o‡ (MPa$\sqrt{m}$)	Pore Type
C1	0.100	15,708	4.36	Shrinkage
C5	0.125	24,544	4.68	Shrinkage
B1	0.300	141,372	9.65	Spherical
B2	0.390	238,918	10.66	Shrinkage
B3	0.085	11,349	4.99	Shrinkage
B4	0.200	62,832	7.15	Spherical
D5	0.250	98,175	6.33	Shrinkage

† C - Standard Weld; B - Squeezed Weld; D - Vibrated Weld

* from assumed semi-circular or circular pore area as discussed in Section 3.6

‡ $K_o = 1.12*(2\sigma/\pi)*\sqrt{(\pi r)}$

FIGURES

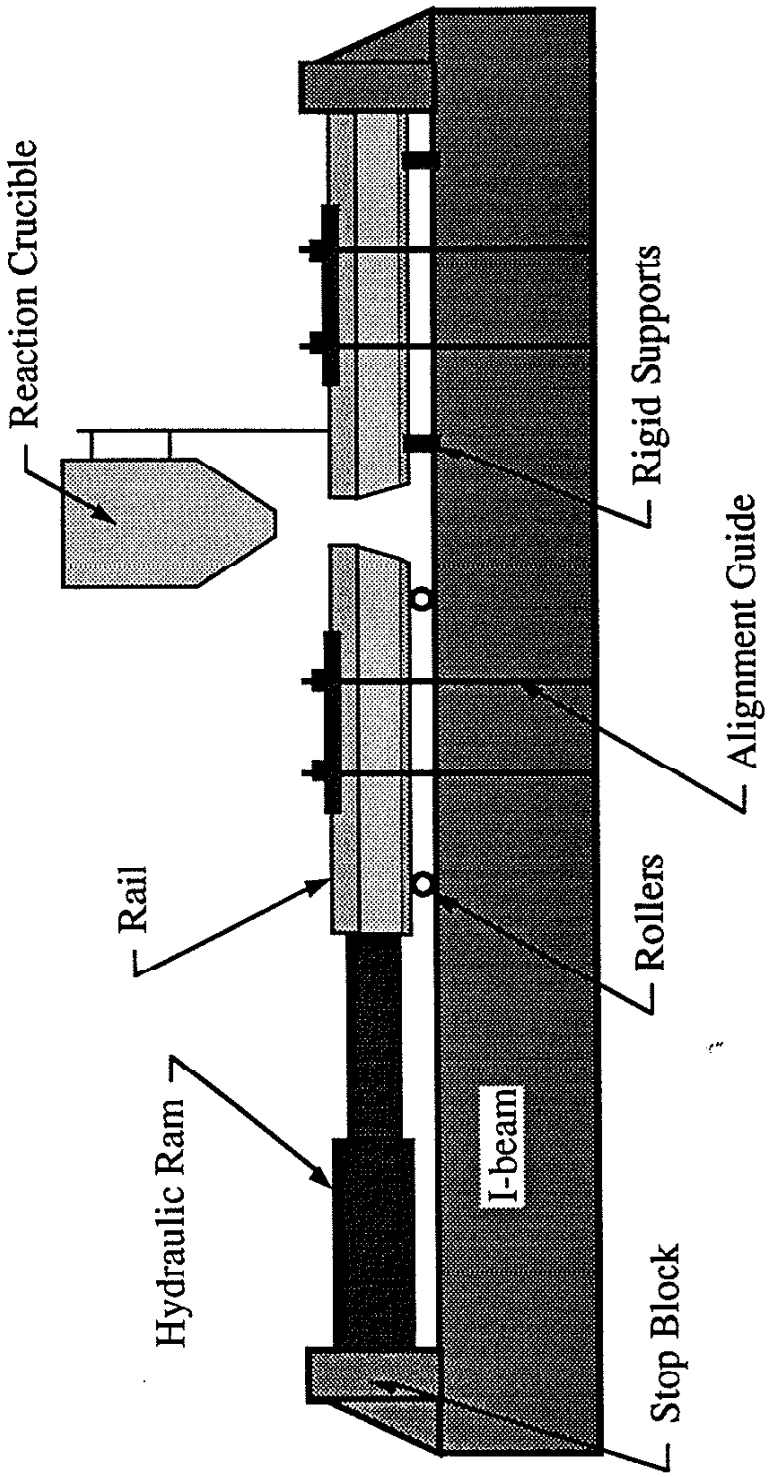

Figure 1. I-Beam Welding Fixture (mold removed).

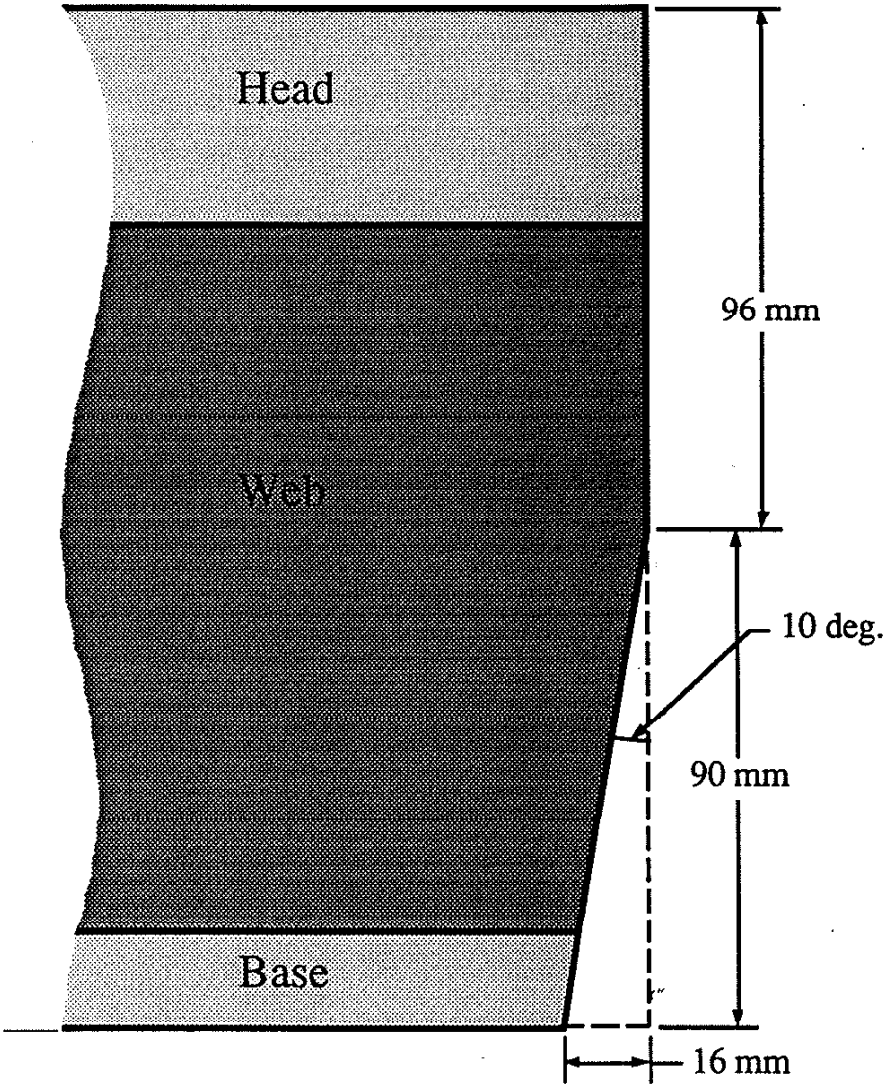

Figure 2. Detail of Rail End Bevel.

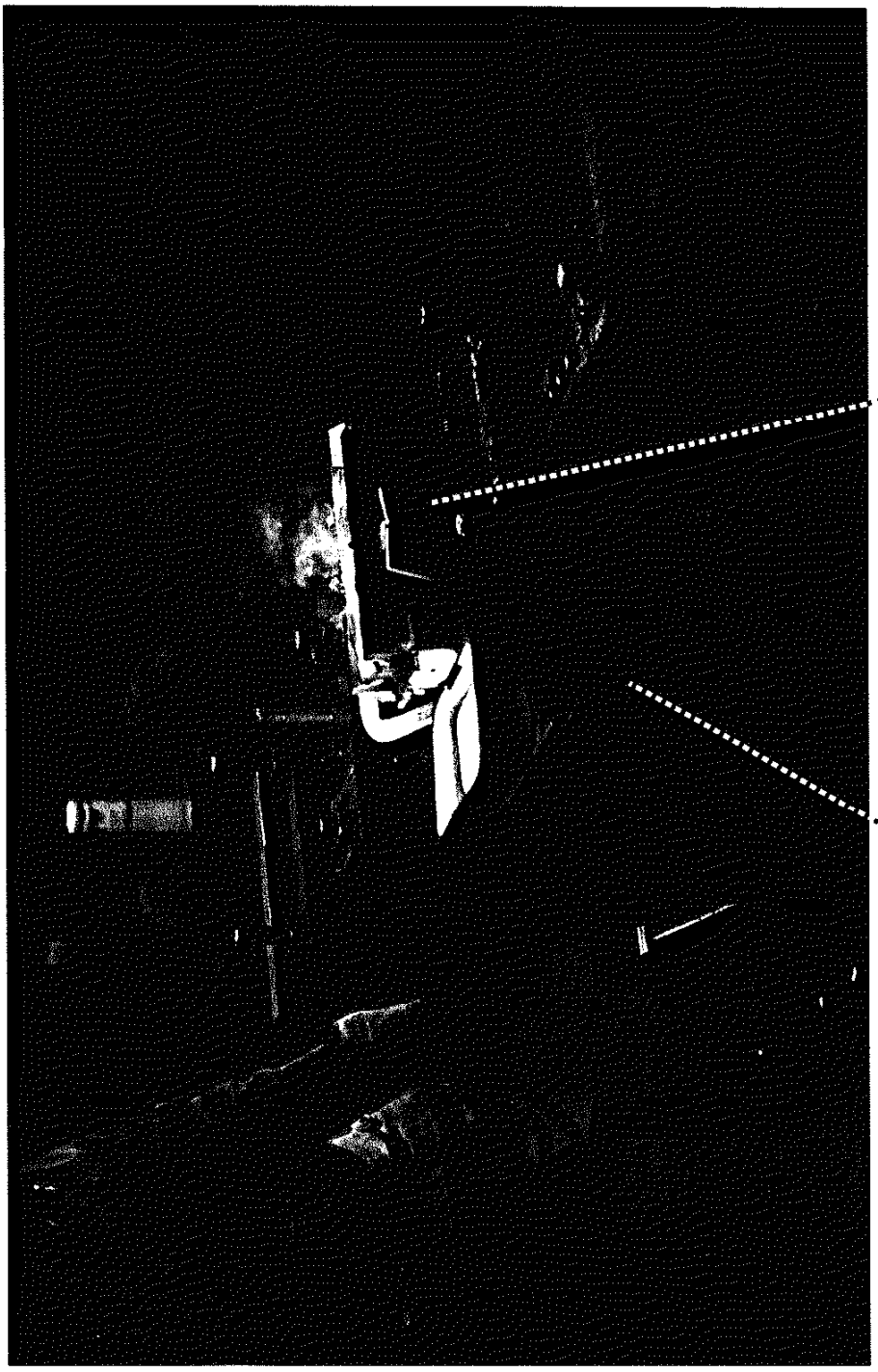

Figure 3. Photo of Mold and Leak Preventing Apparatus.

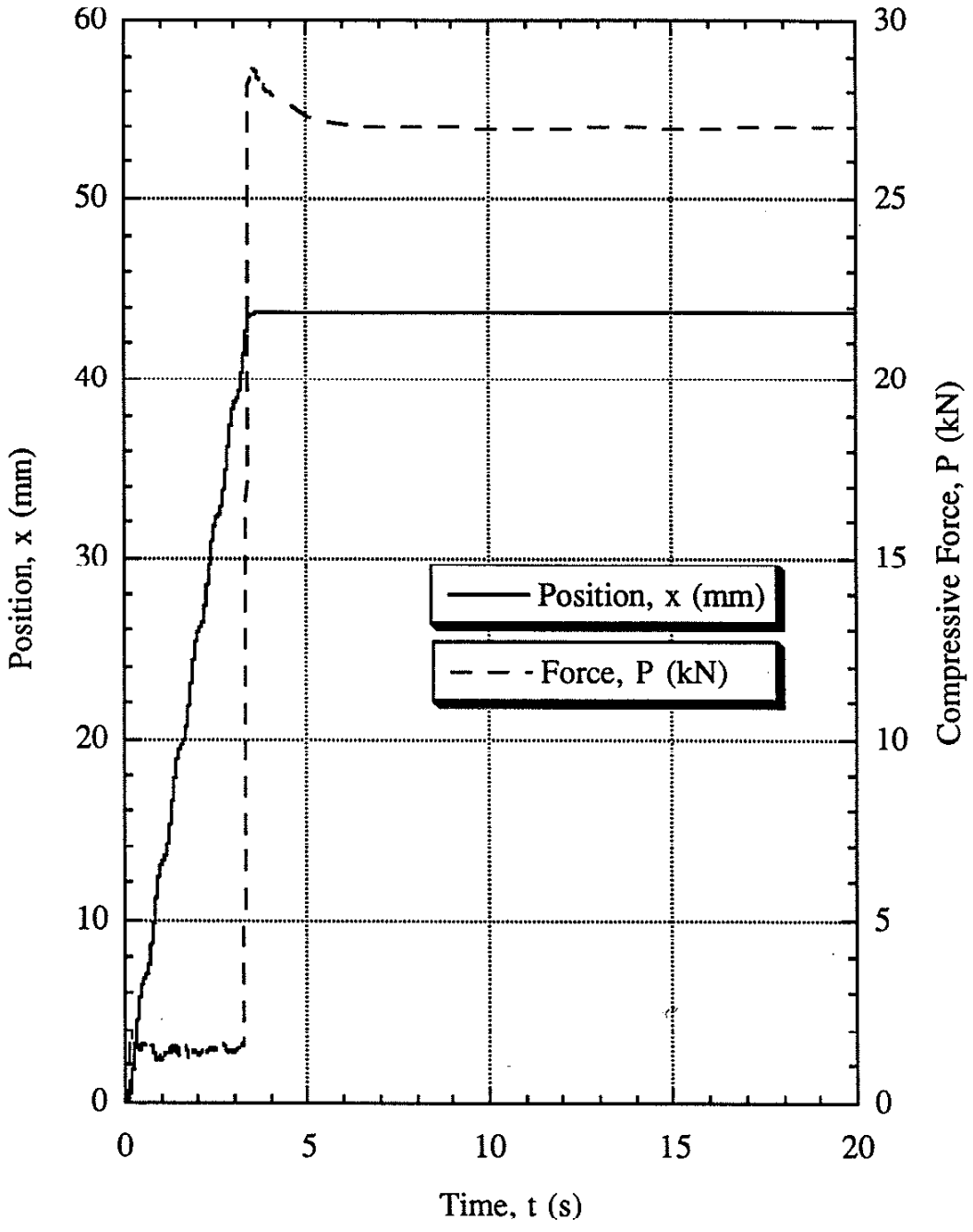

Figure 4. Compressive Force and Displacement During Squeezed Weld.

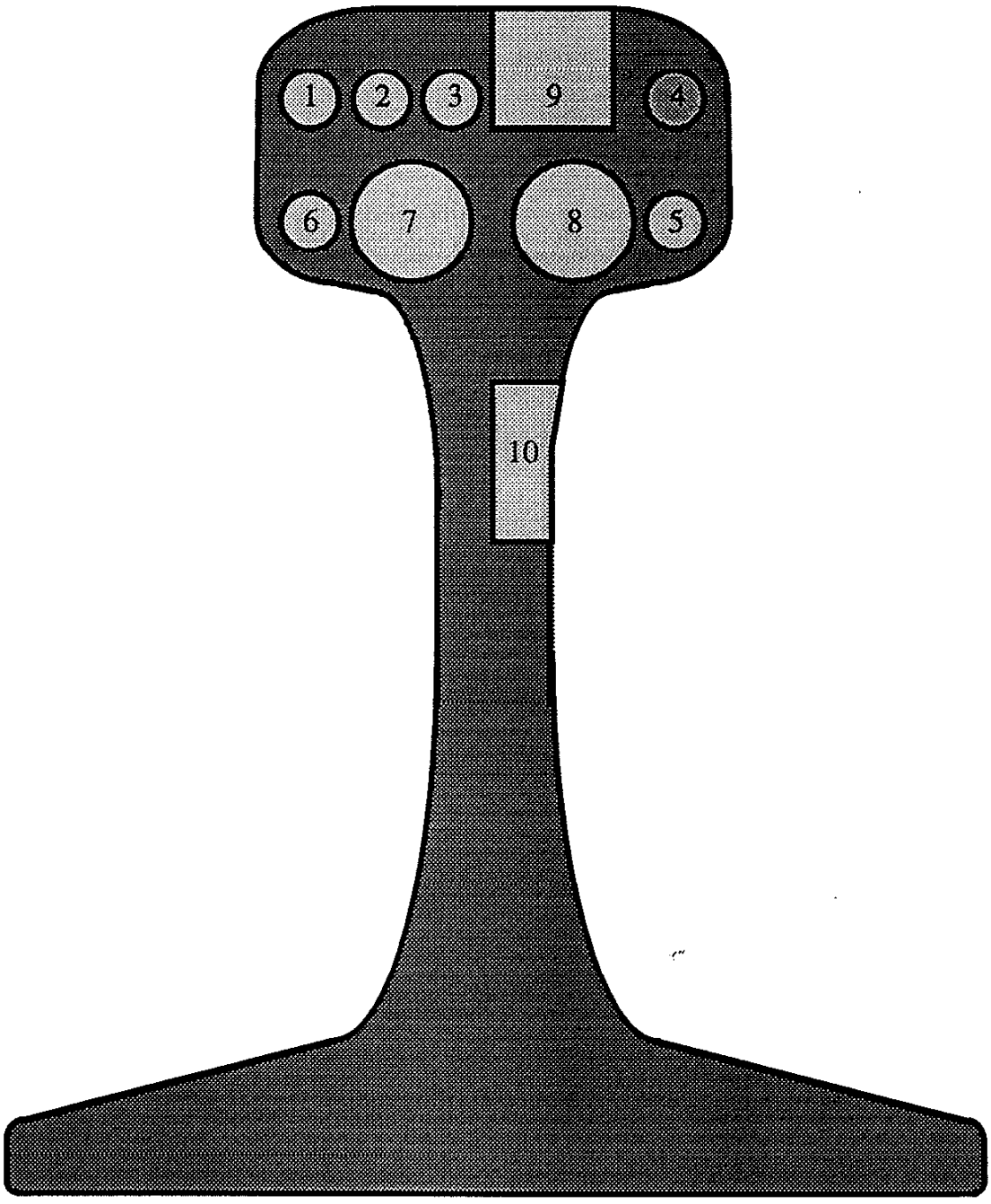

Figure 5. Location of Weld Specimens in 136 RE Cross-Section
(specimens : 1-6 fatigue, 7-8 tensile, 9-10 metallography).

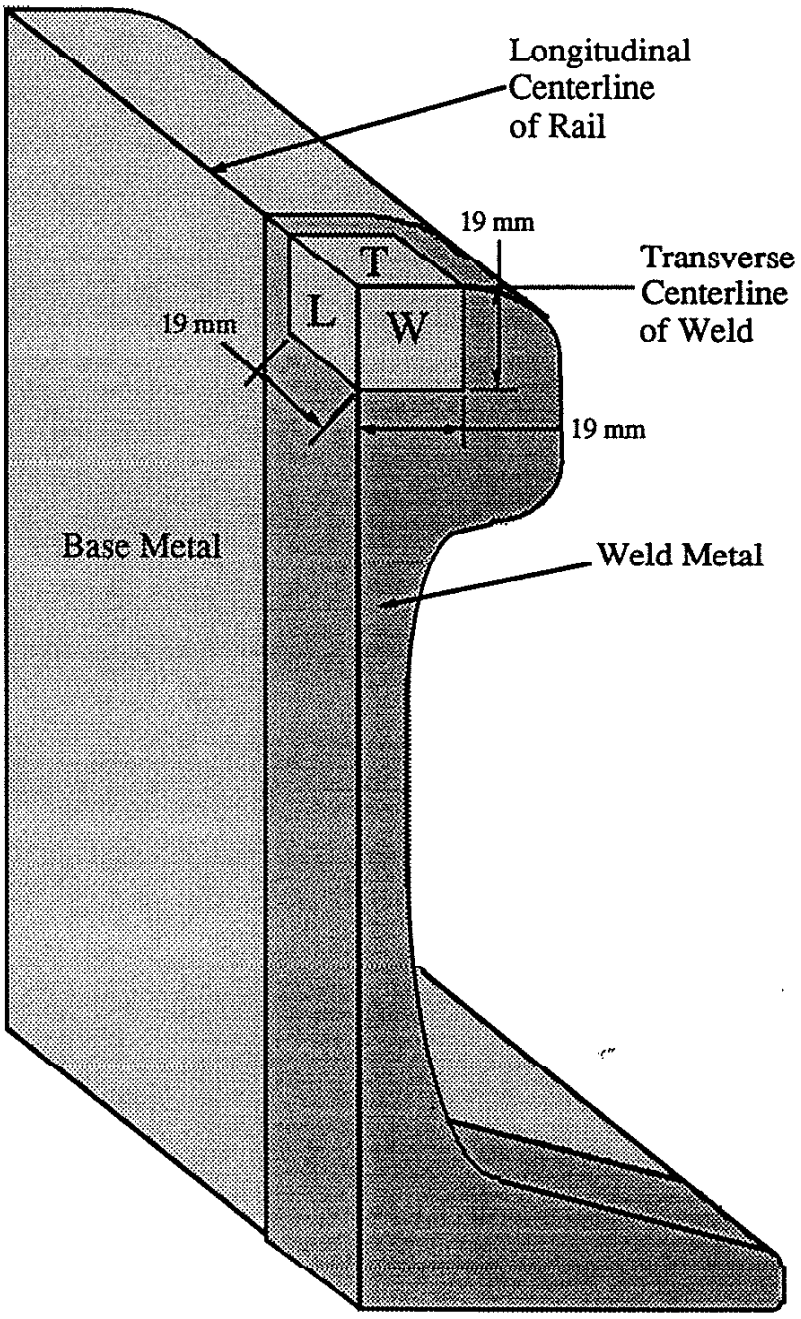

Figure 6. Orientation of Confocal Microscopy Specimens.

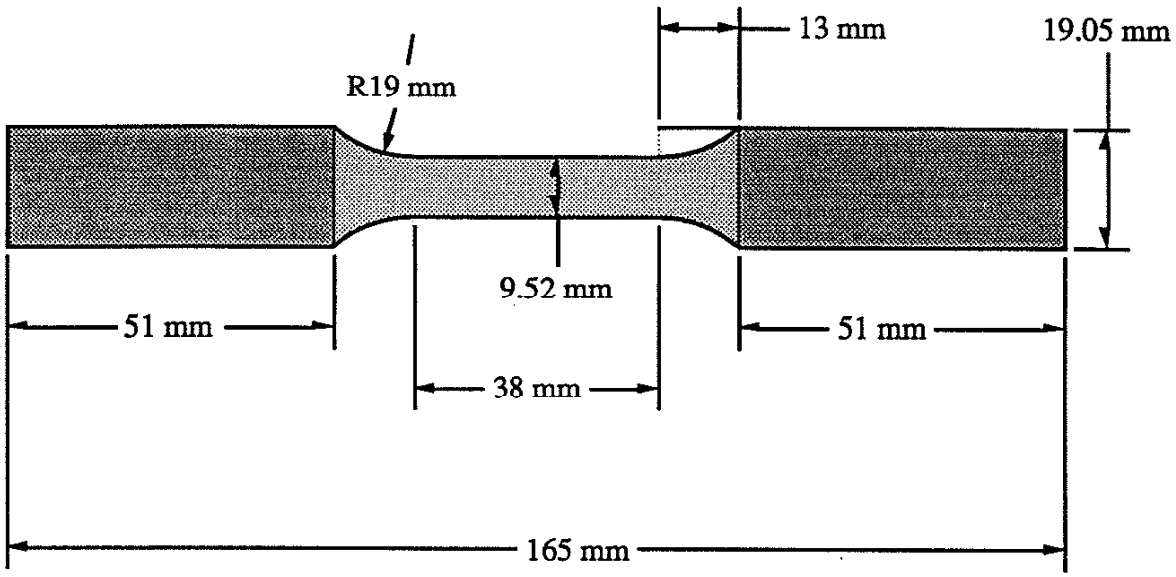

Figure 7. Tensile Specimen Dimensions.

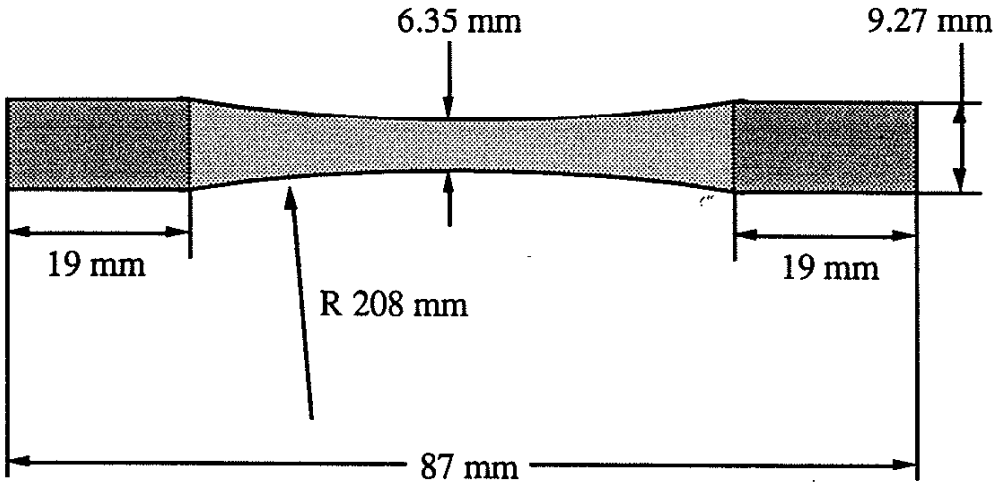

Figure 8. Fatigue Specimen Dimensions.

(a) standard weld

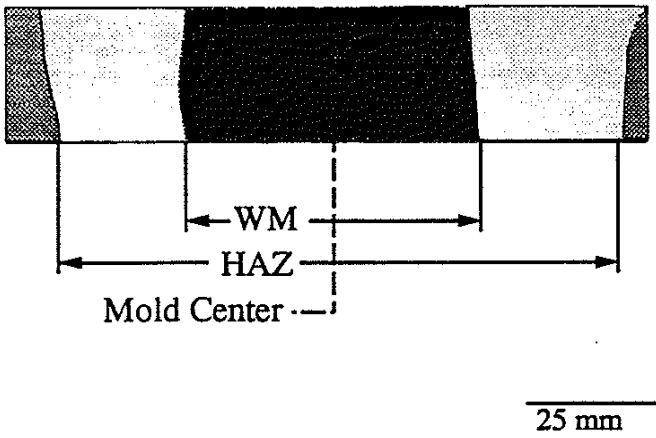

(b) squeezed weld

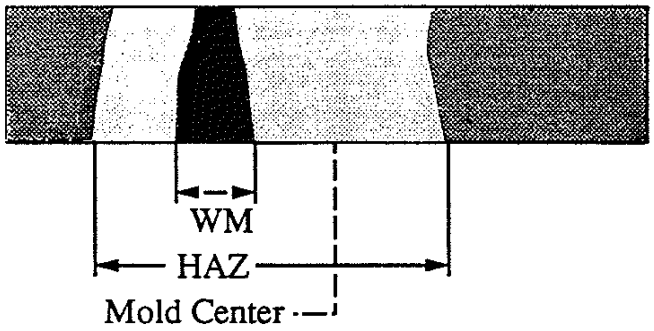

(c) vibrated weld

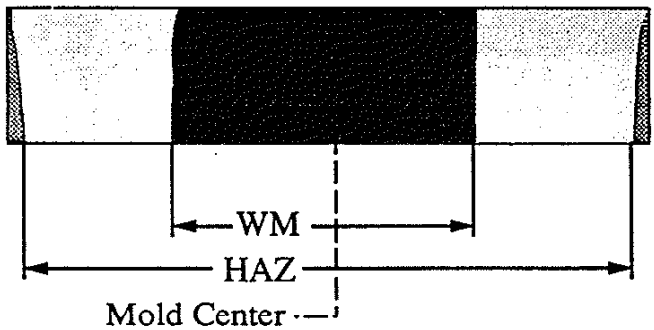

Figure 9. Longitudinal Metallograpic Sections of Welds (tracings of micrographs).

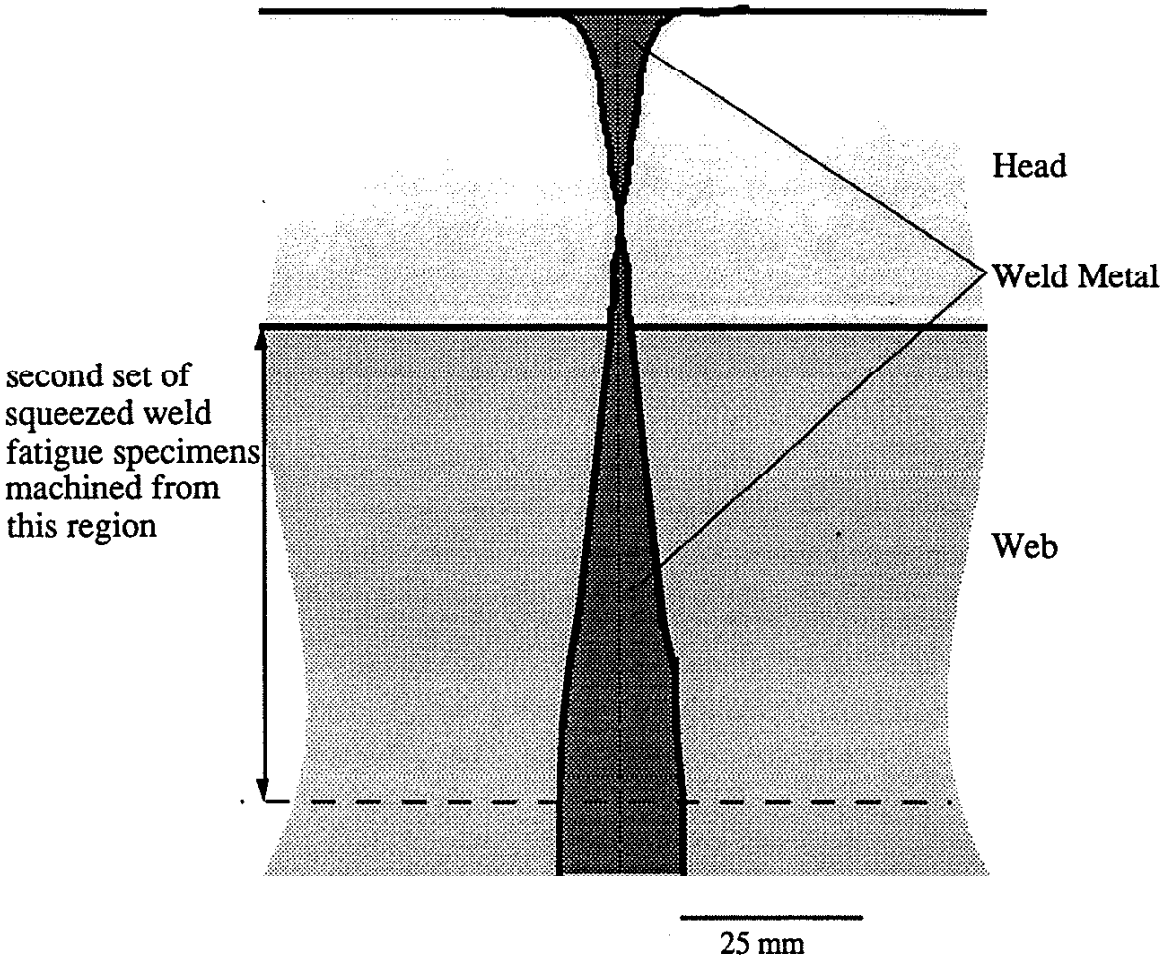

Figure 10. Squeezed Weld Profile.

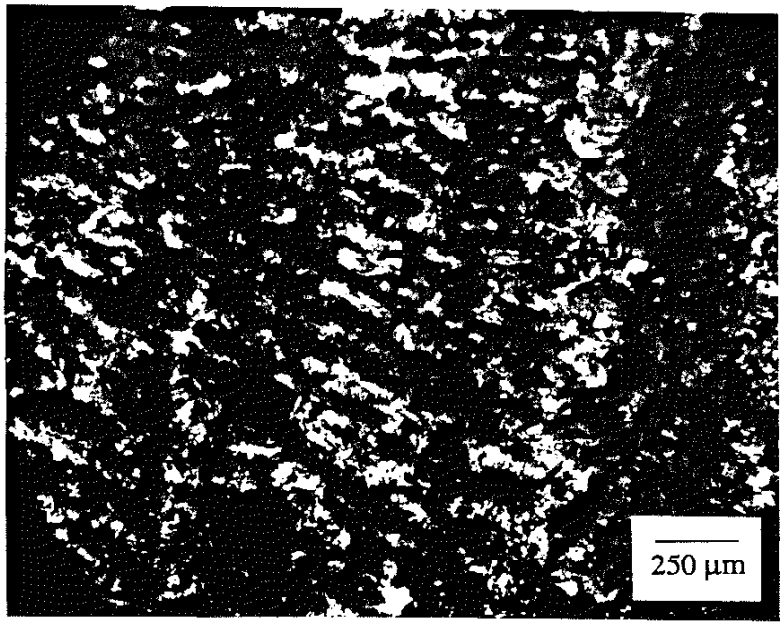

a) line of fusion etched in Kalling's Reagent

b) weld metal etched in 2% Nital

Figure 11. Microstructure of Standard Weld.

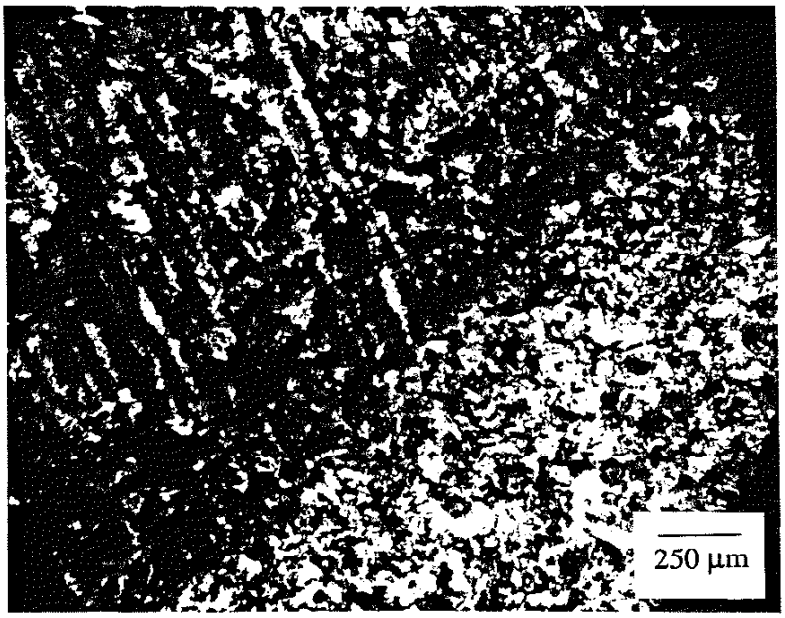

a) line of fusion etched in Kalling's Reagent

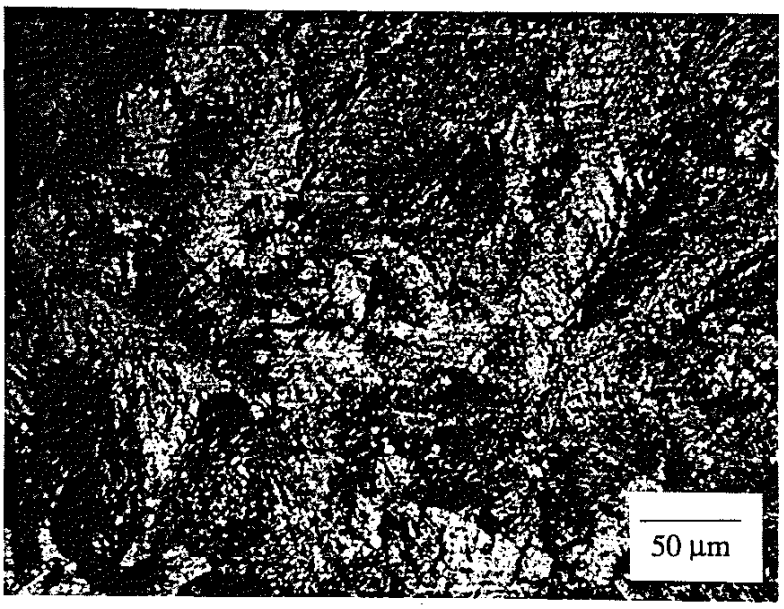

b) weld metal etched in 2% Nital

Figure 12. Microstructure of Squeezed Weld.

a) line of fusion etched in Kalling's Reagent

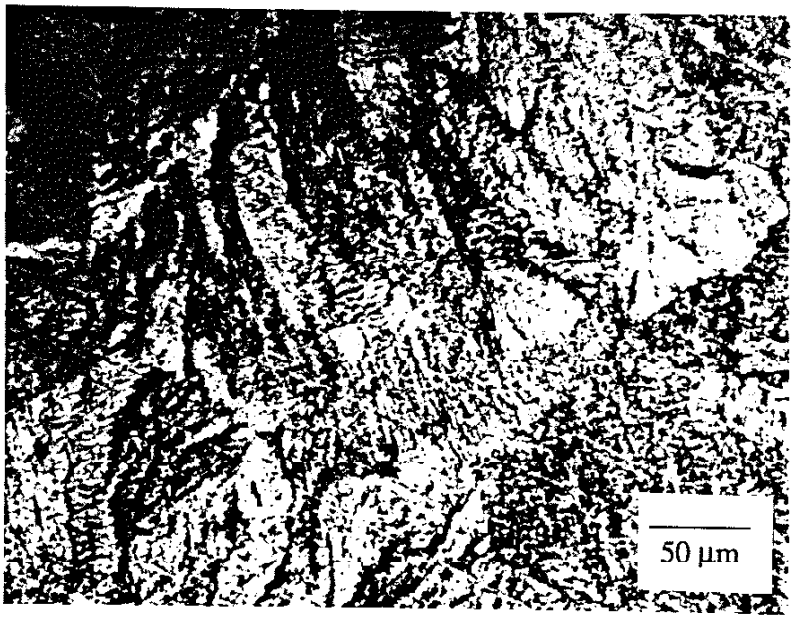

b) weld metal etched in 2% Nital

Figure 13. Microstructure of Vibrated Weld.

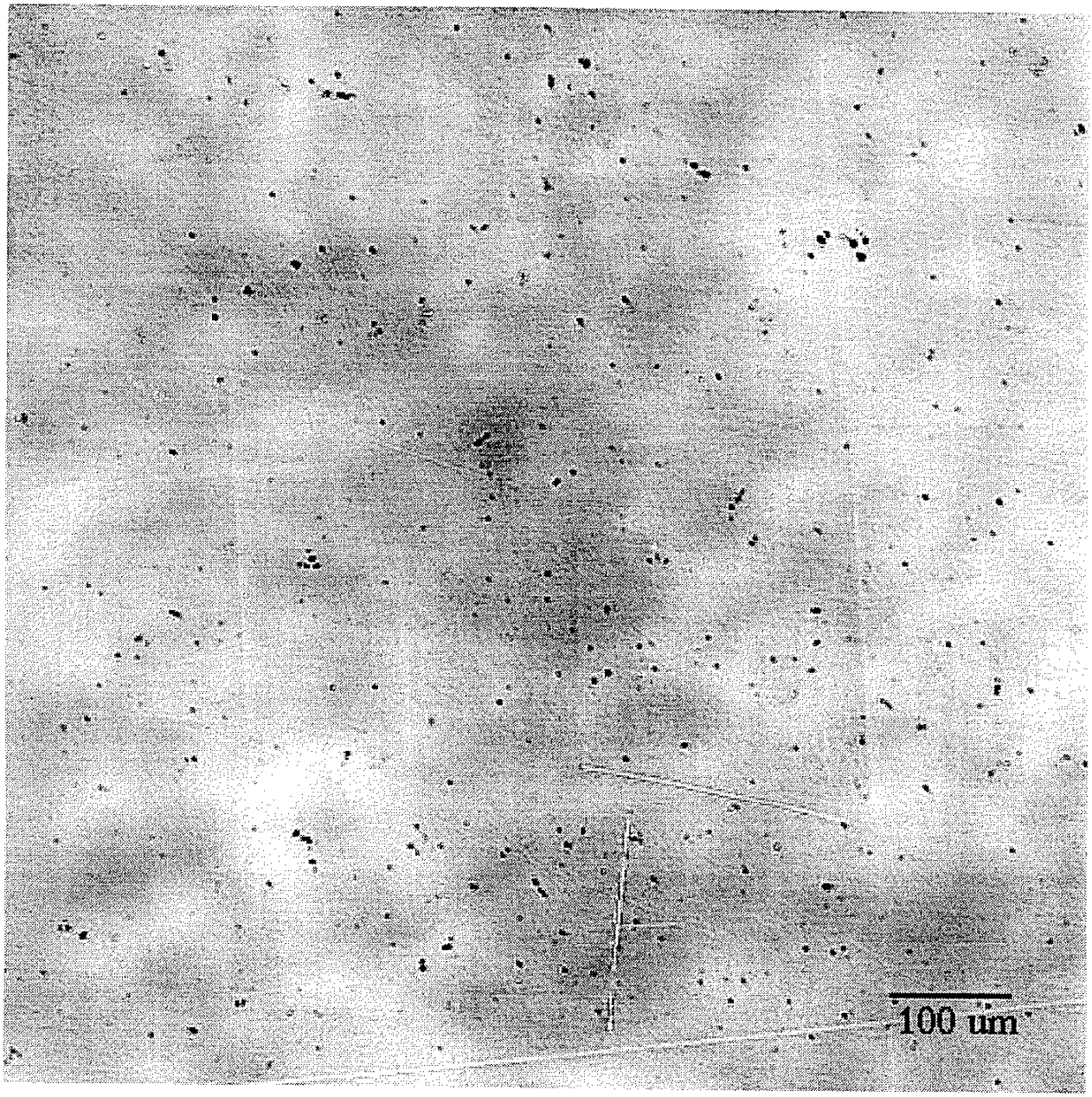

Figure 14. Confocal Image of Standard Weld (longitudinal face).

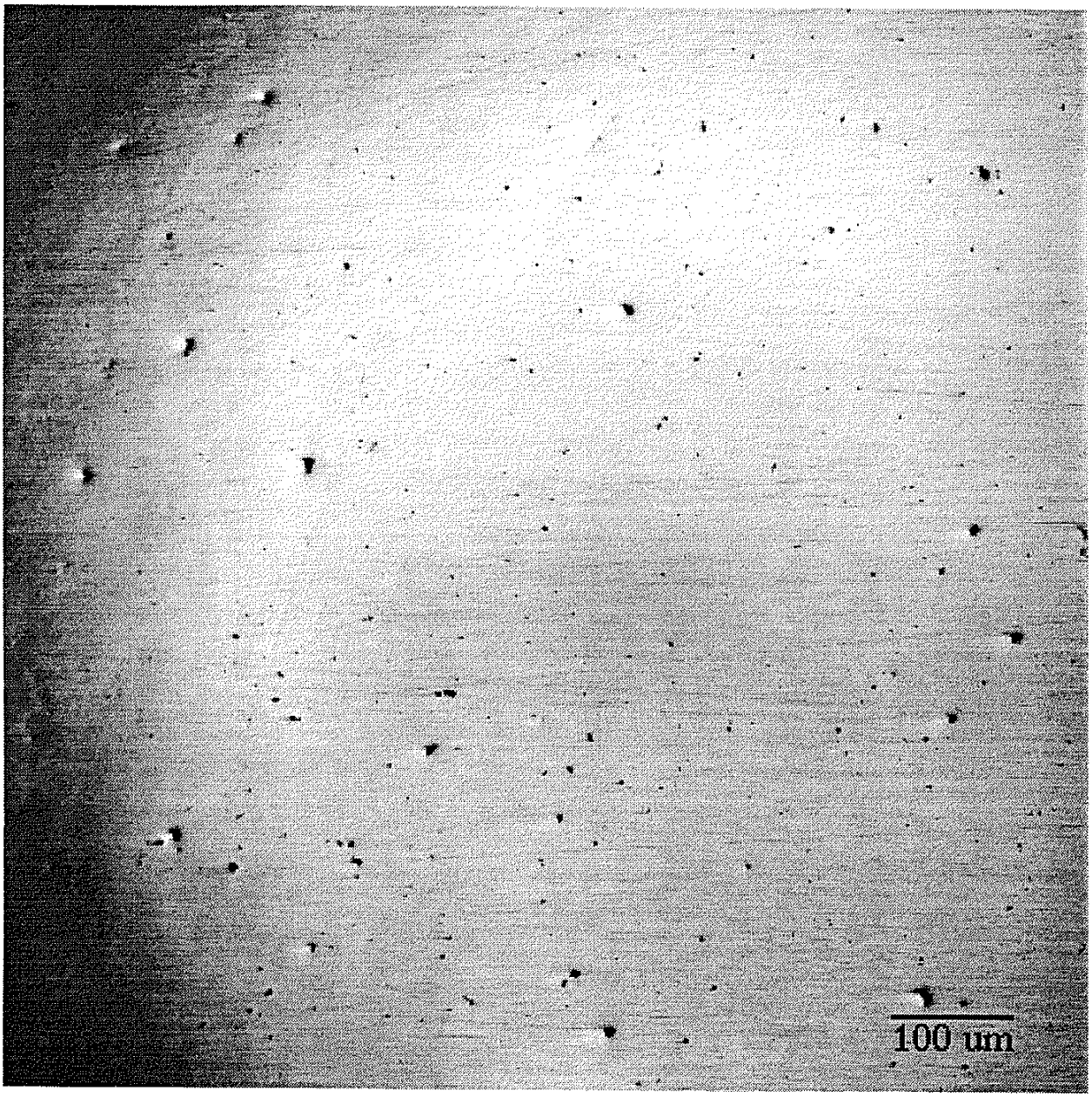

Figure 15. Confocal Image of Squeezed Weld (longitudinal face).

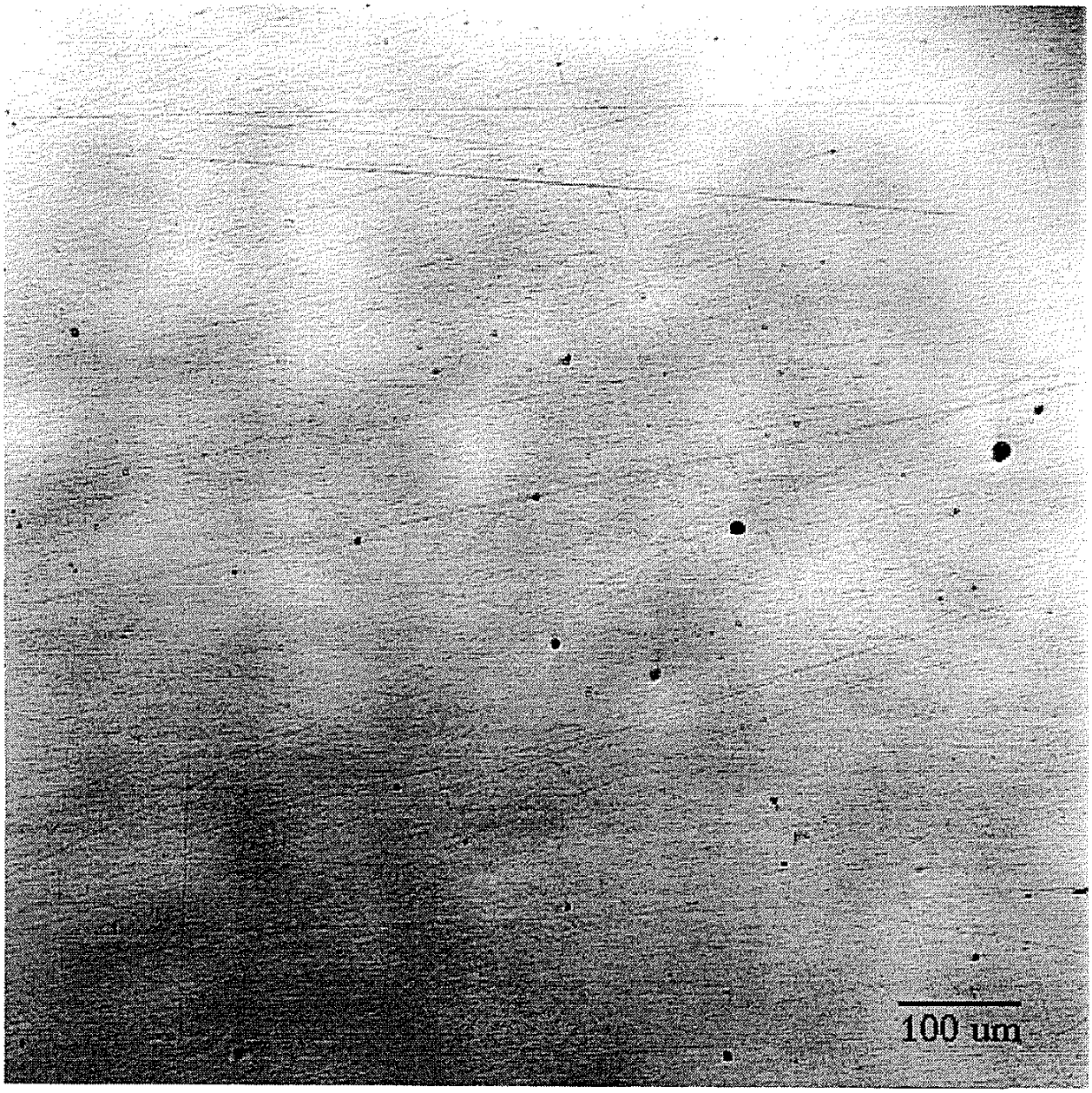

Figure 16. Confocal Image of Vibrated Weld (longitudinal face).

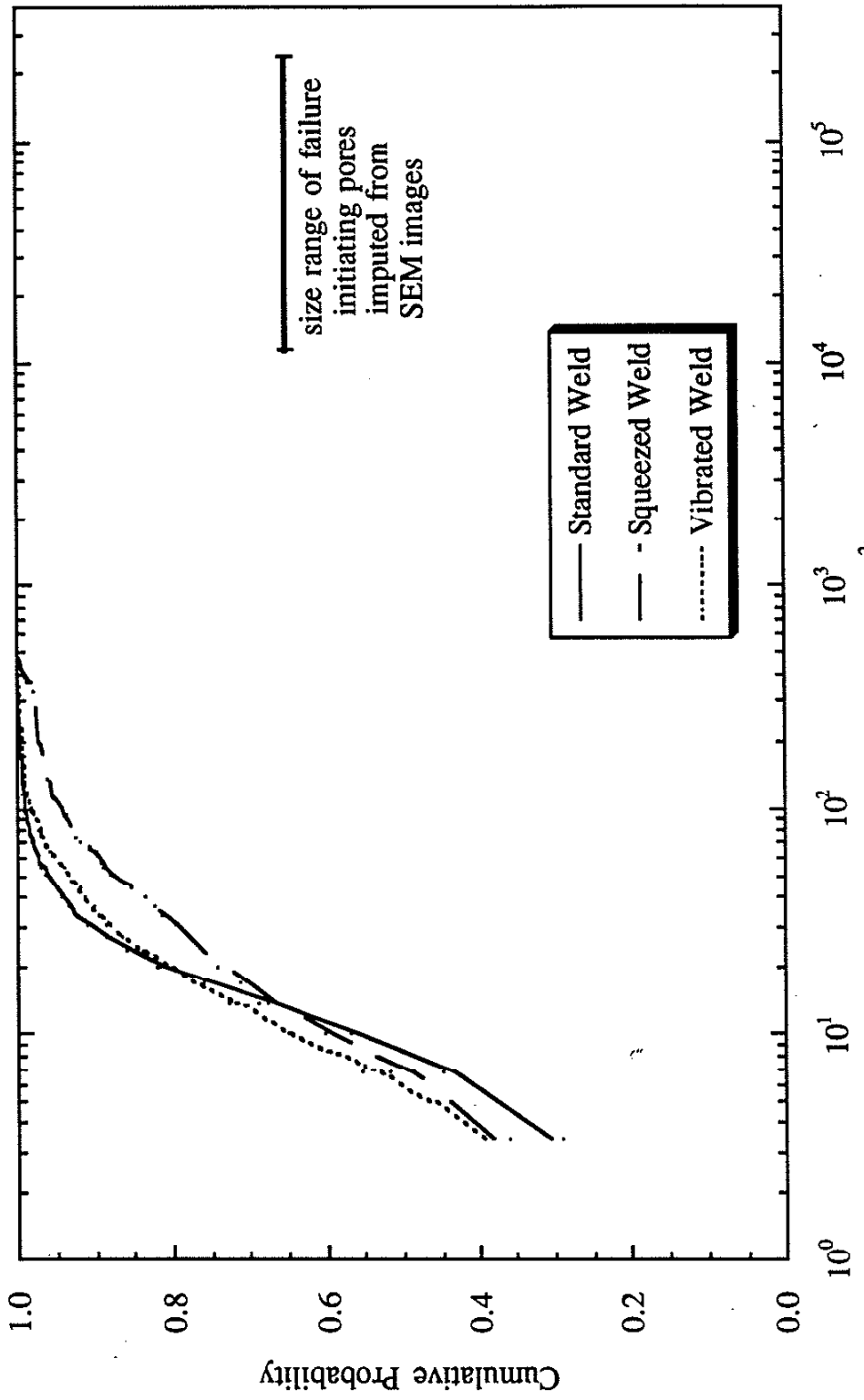

Figure 17. Cumulative Probability versus Pore Size.

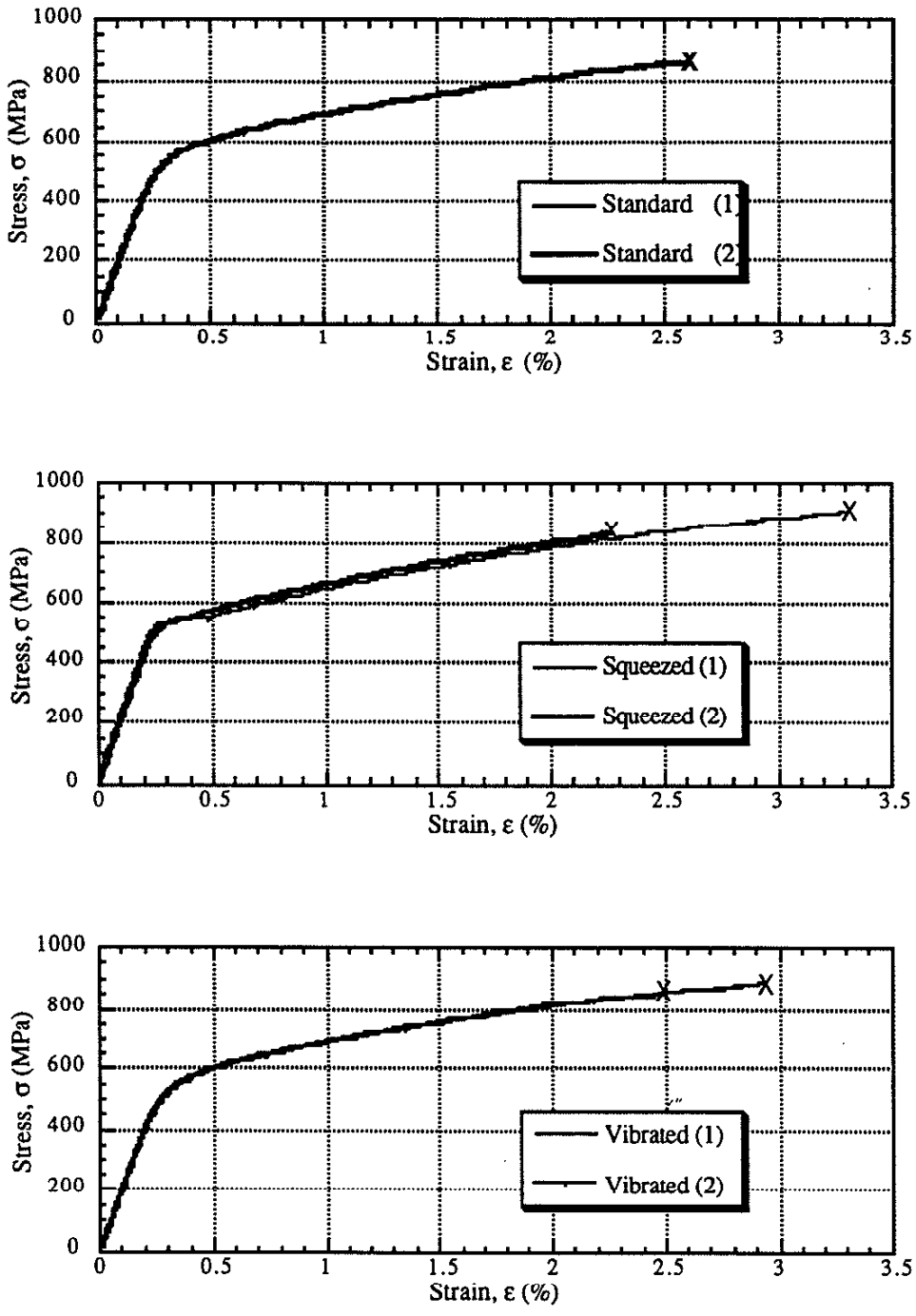

Figure 18. Stress-Strain Curves from Tensile Tests (top : standard weld, middle : squeezed weld-HAZ, bottom : vibrated weld).

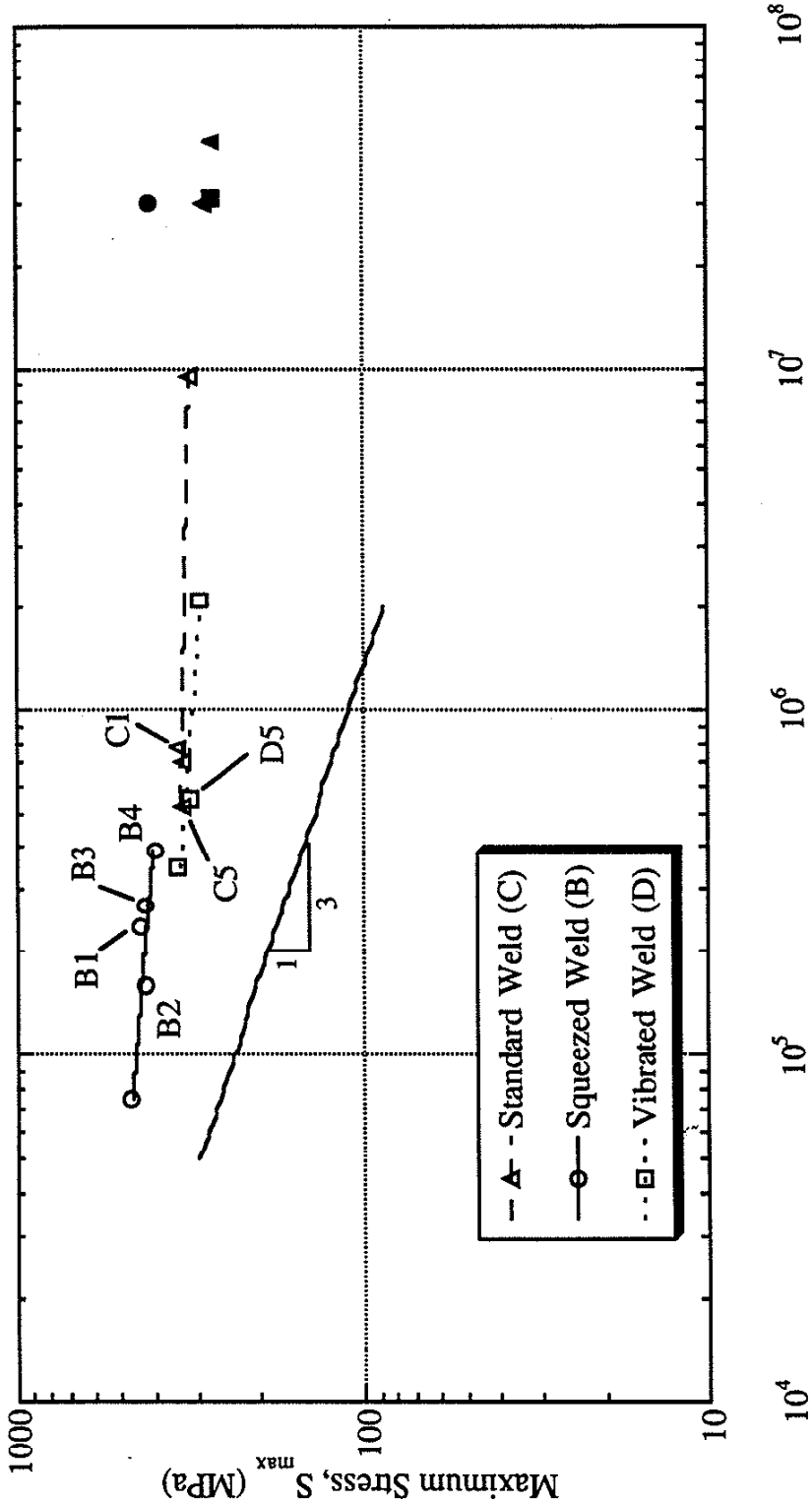

Figure 19. Fatigue Test Results [shaded symbols denote runouts]; (Labeled points correspond to specimens discussed in Section 3.6 - Fractography).

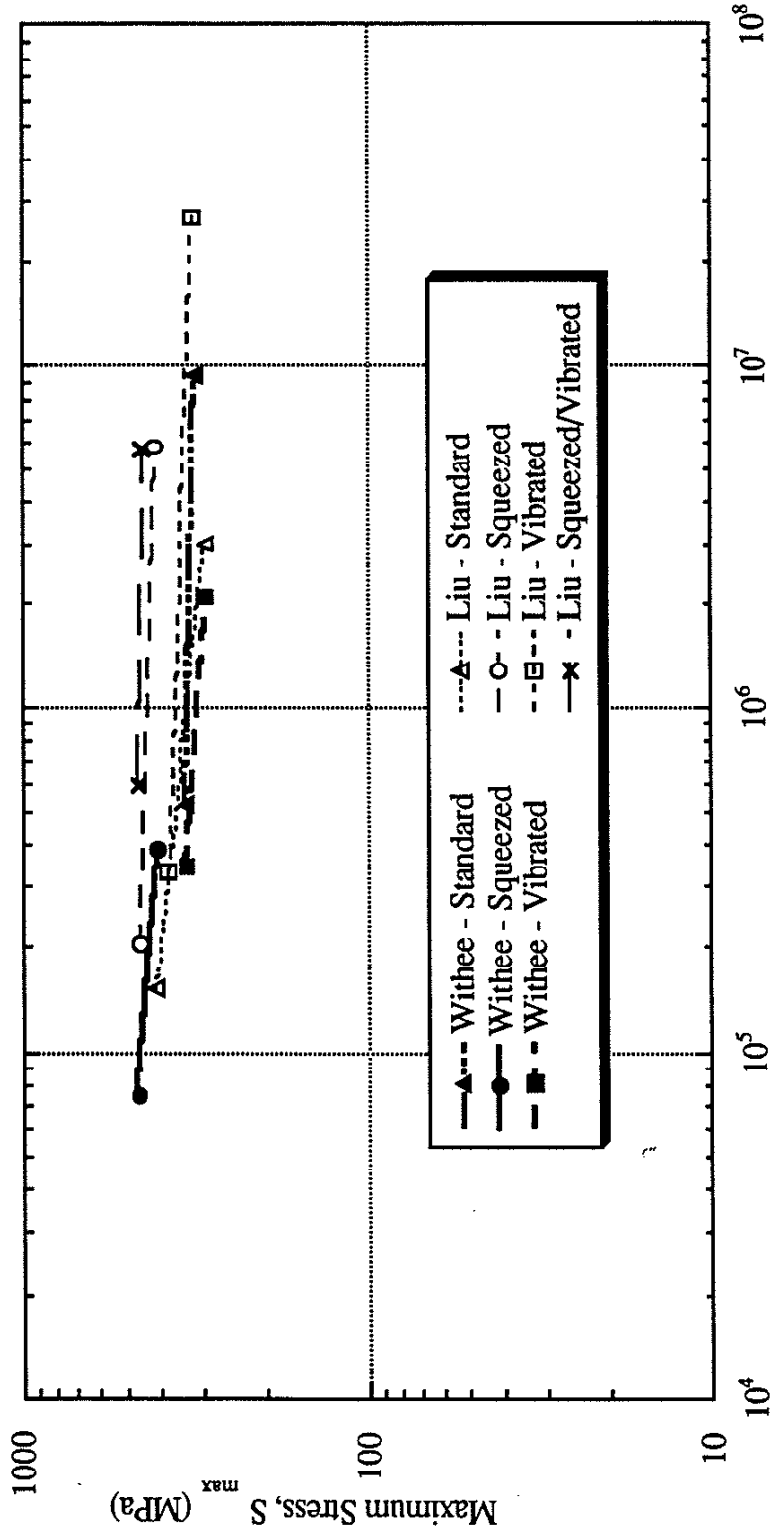

Figure 20. Fatigue Data Comparison (shown are best fit lines to test data).

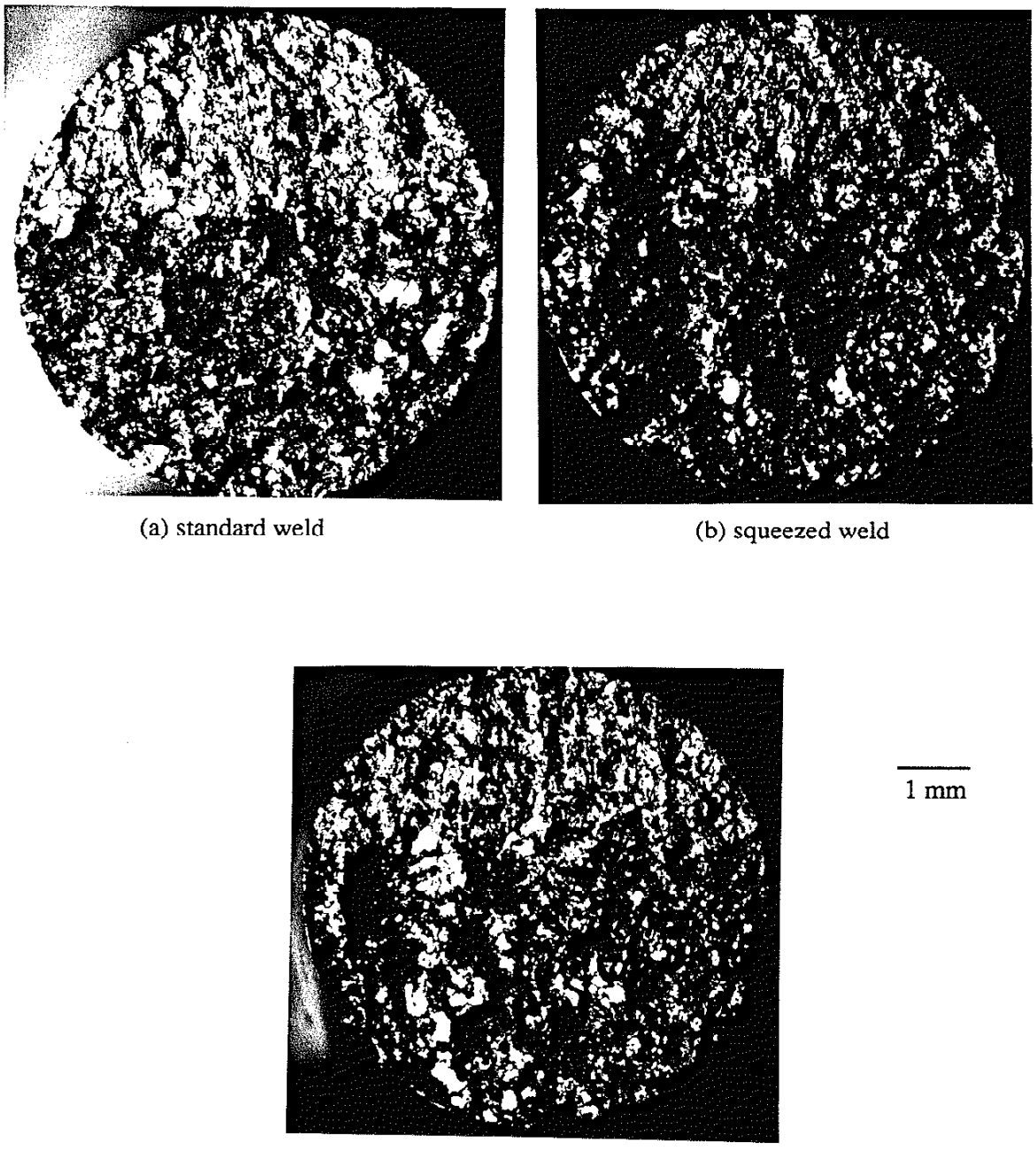

(a) standard weld

(b) squeezed weld

(c) vibrated weld

Figure 21. Optical Images of Fatigue Specimen Fracture Surfaces.

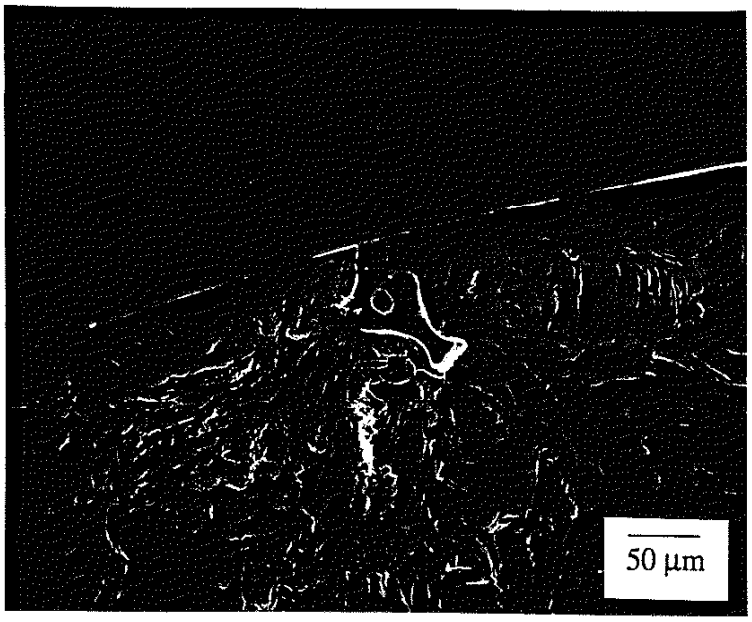

Figure 22. SEM Image of Fracture Surface for Standard Weld Fatigue Specimen C1.

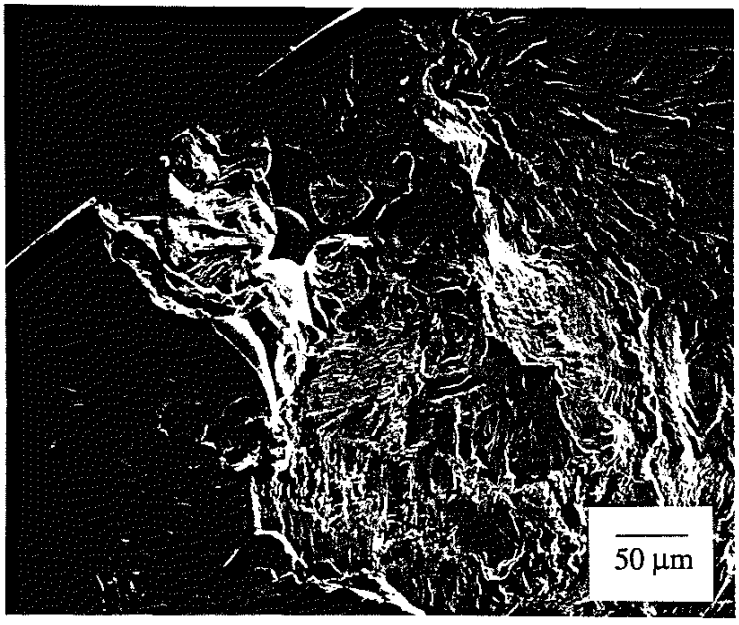

Figure 23. SEM Image of Fracture Surface for Standard Weld Fatigue Specimen C5.

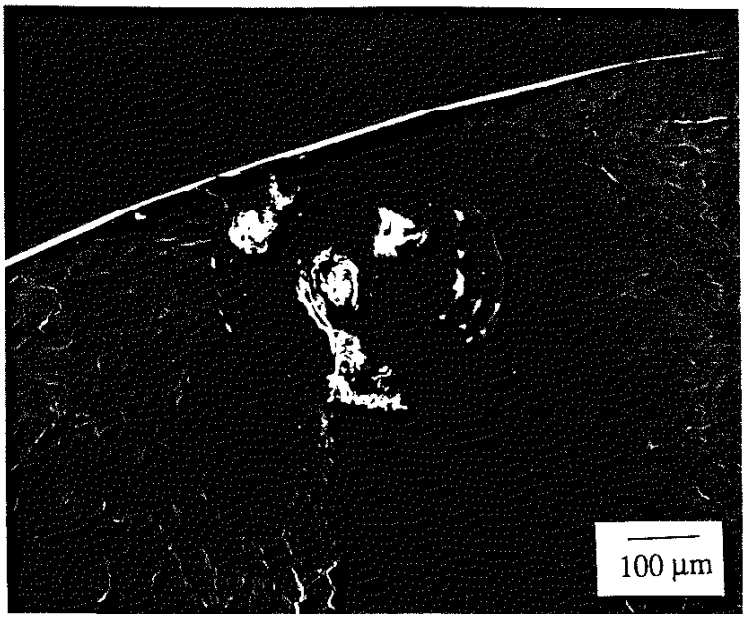

Figure 24. SEM Image of Fracture Surface for Squeezed Weld Fatigue Specimen B1.

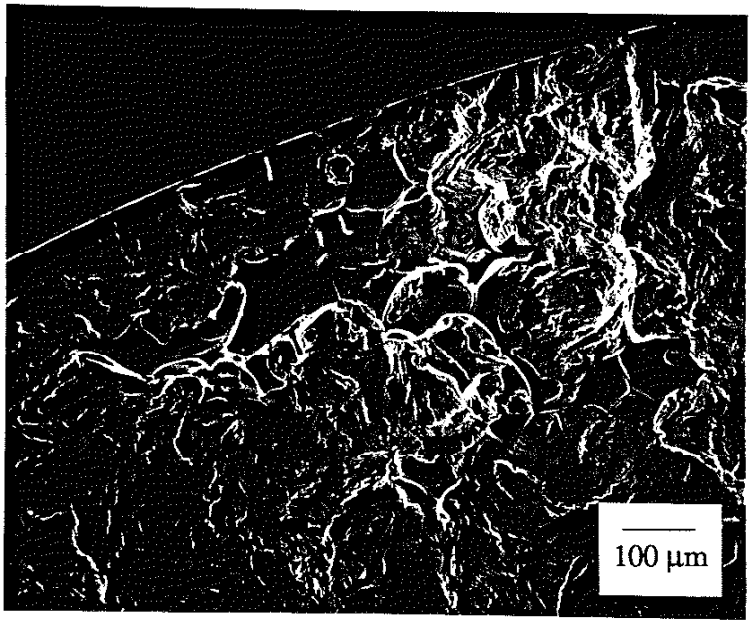

Figure 25. SEM Image of Fracture Surface for Squeezed Weld Fatigue Specimen B2.

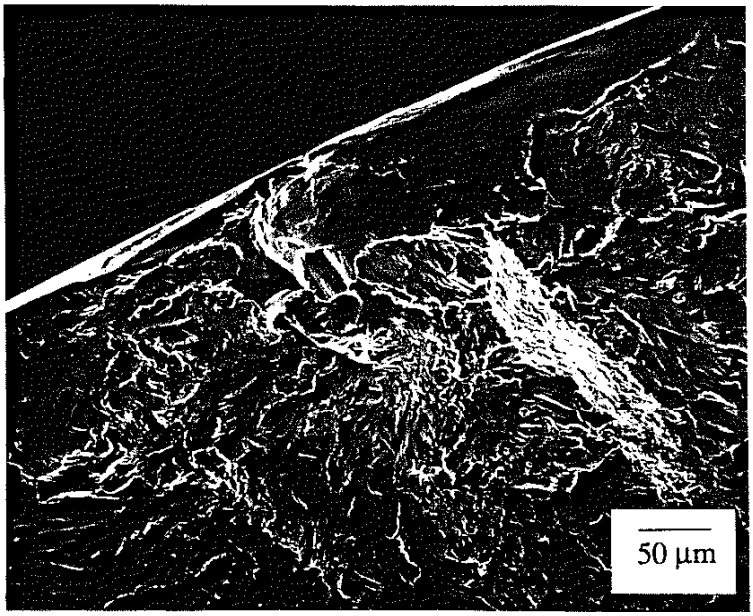

Figure 26. SEM Image of Fracture Surface for Squeezed Weld Fatigue Specimen B3.

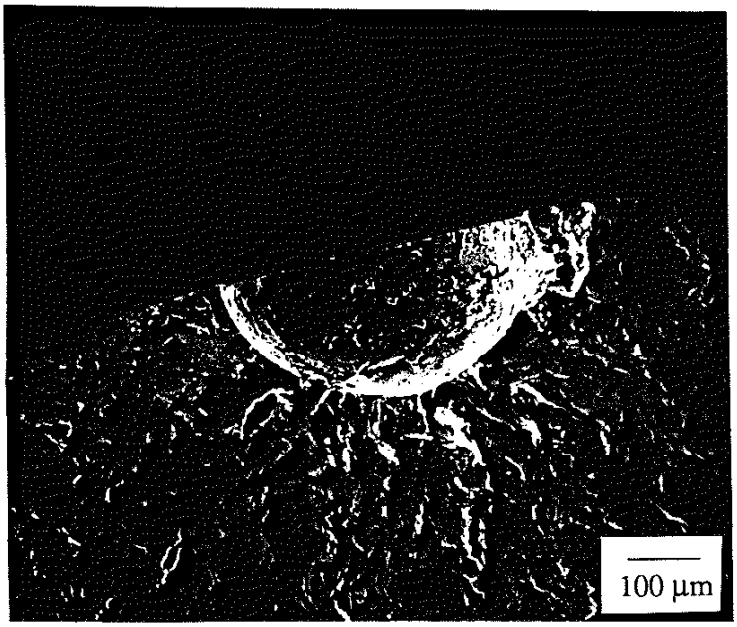

Figure 27. SEM Image of Fracture Surface for Squeezed Weld Fatigue Specimen B4.

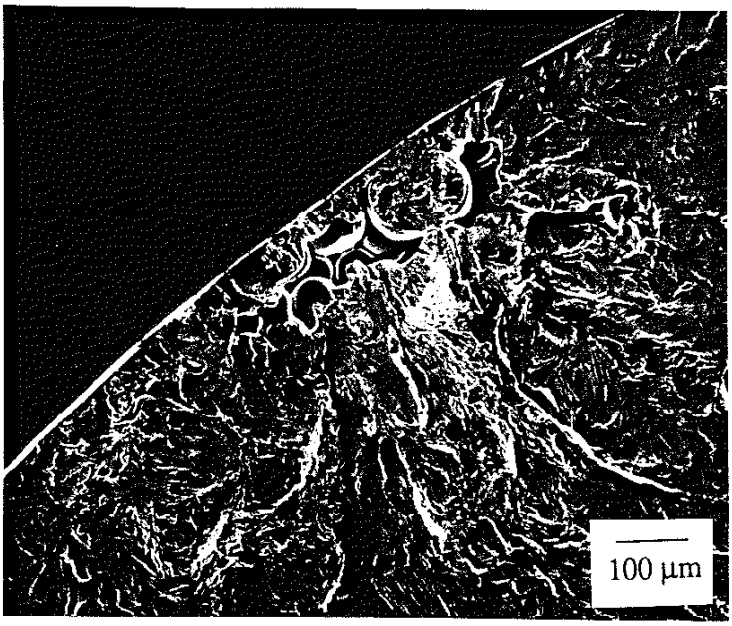

Figure 28. SEM Image of Fracture Surface for Vibrated Weld Fatigue Specimen D5.

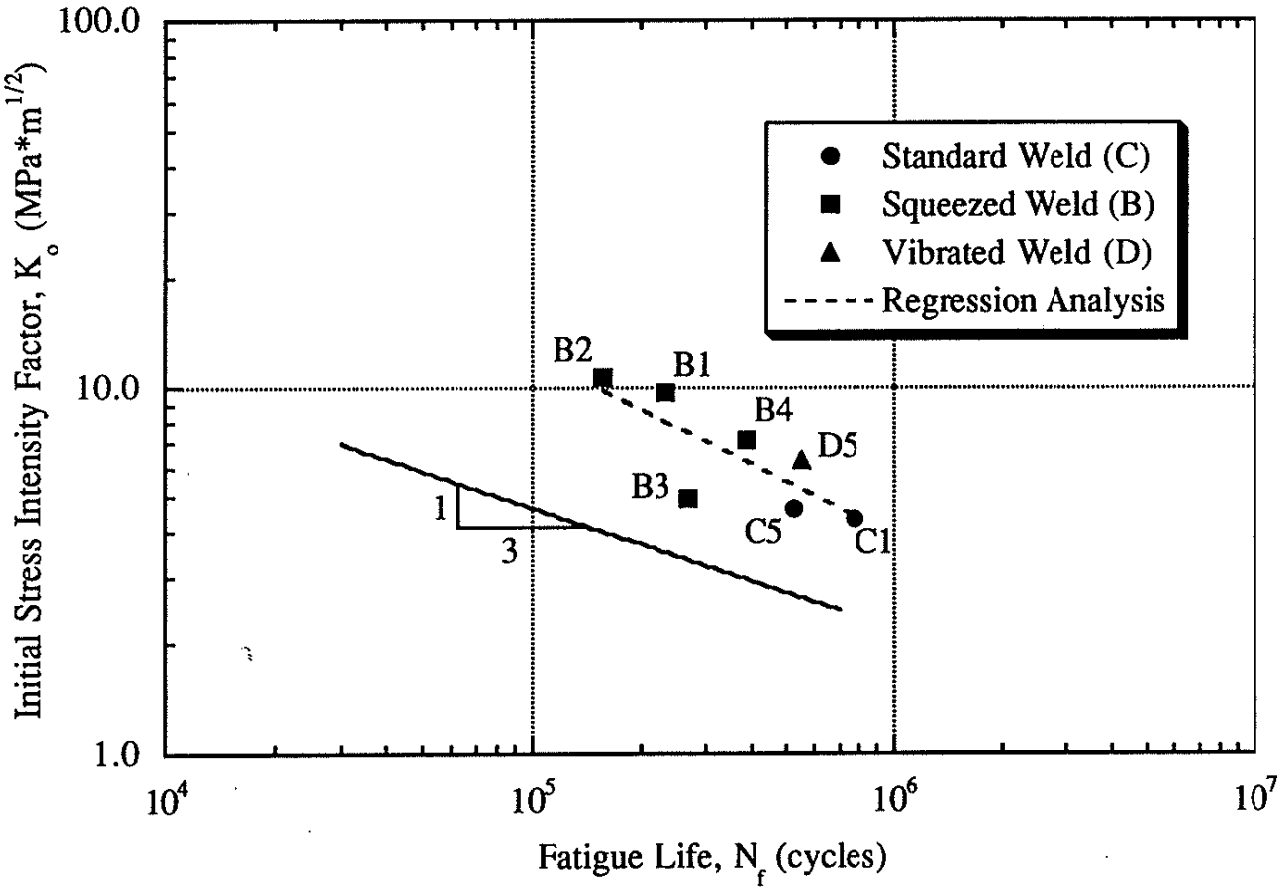

Figure 29. Initial Stress Intensity Factor of Pores Initiating Failure; (Labeled points correspond to specimens discussed in Section 3.6 - Fractography).

LIST OF REFERENCES

Fricke, H. D. "Thermit Welding of Yard Tracks" *Plant Engineering* 22 March 1984: 61-62.

Fry, Gary T. "A Modified Thermite Rail Welding Procedure." MS Thesis. University of Illinois at Urbana-Champaign, 1992.

Gibert, F. "Thermit-Welding of Rails: Old Recipe for Modern Track." *Rail International* May 1988: 8-11.

Hauser, Daniel. "Welding of Railroad Rails-A Literature and Industry Survey." *Rail Steels-Developments, Processing, and Use* Proceedings of the American Society for Testing and Materials Committee A-1. (ASTM STP-644). 17-18 December 1976. Ed. D. H. Stone and G. G. Knupp. Philadelphia: American Society for Testing and Materials, 1978. 118-141.

Jha, Bijendra. "Thermite Welding of Rail Steel." PhD Diss. Illinois Institute of Technology, 1989. Ann Arbor: UMI, 1989. 9027309

Key, A. J. "The THERMIT® Process for Railwelding." *Metal Construction* July 1984: 419-422.

Kramer, Jerome. "Thermite Welds: Getting Ready for Heavier Loads." *Railway Track & Structures* December 1993: 16-20.

Kramer, Jerome. "Thermite Welding Changes Pay Off." *Railway Track & Structures* January 1996: 21-23.

Lange, D. A., H. M. Jennings, and S. P. Shah. "Analysis of Surface Roughness Using Confocal Microscopy." *Journal of Materials Science* 15 July 1993: 3879-3884.

Liu, Wei. "Microstructures and Mechanical Properties of Standard and Modified Thermite-Welded Railroad Rails." MS Thesis. University of Illinois at Urbana-Champaign, 1994.

Lonsdale, Cameron P. "Evaluation of Grain Refinement Techniques in Thermite Railroad Rail Welds," MS Thesis. Case Western Reserve University, 1992.

Moin, Ebrahim. "The Current Status of Field Welding of Rail." *Railway Track & Structures* October 1988: 30.

"New Ways to Improve Field-Weld Quality." *Railway Track & Structures* September 1990: 31-33.

Schroeder, L. C. and D. R. Poirier. "Thermite Rail Welds; The Process, Mechanical and Metallurgical Properties, and Possible Improvements." *Railroad Rail Welding.* Proceedings of the Association of American Railroads. 29-30 November 1983. Association of American Railroads, 1985. 21-59.

Siljander, Aslak and Frederick V. Lawrence, Jr. "The Mechanical Properties of AL-Si 319: The Role of Casting Porosity." University of Illinois at Urbana-Champaign, 8 April 1988.

Siska, Peter C. "The Effect of Sonic Power Vibrations on Solidifying Thermit Welds." MS Thesis. The Ohio State University, 1980.

Sun, Jian, et al. "Progress in Development of Squeeze Welding Process." Association of American Railroads Research and Test Department. Chicago, IL: June 1994.